

**The Impact of Trade-wind Strength on Precipitation
over the Windward Side of the Island of Hawaii**

Mary Ann Esteban and Yi-Leng Chen¹

Department of Meteorology

School of Ocean and Earth Science and Technology

University of Hawaii

Honolulu, HI 96822

June 2007

¹Corresponding author address: Dr. Yi-Leng Chen, Department of Meteorology, SOEST,
University of Hawaii at Manoa, Honolulu, HI 96822, E-mail: yileng@hawaii.edu

ABSTRACT

The effects of trade-wind strength and the diurnal heating cycle on the production of summer trade-wind rainfall on the windward side of the island of Hawaii are examined from the data collected from the Hawaiian Rainband Project (HaRP) during 11 July - 24 August 1990 and the National Weather Service Hydronet and National Climatic Data Center rain gauge data during 11 July - 24 August for years 1997-2000.

For strong trades, the daily rainfall totals on the windward lowlands west of Hilo are higher with a nocturnal maximum there due to the convergence of the katabatic flow and the incoming decelerating trade-wind flow, and orographic lifting aloft. The maximum rainfall axis shifts farther inland when trades are stronger. Except in the late afternoon hours, rainfall amounts on the windward side are higher when trades are stronger. For weak trades ($\leq 5 \text{ m s}^{-1}$), the rainfall distributions have a pronounced late afternoon maximum on the windward slopes due to the development of anabatic winds. The nocturnal rainfall over the windward lowlands and the early morning coastal rainfall are lower when trades are weaker.

1. Introduction

The island of Hawaii (Big Island) is the largest of the Hawaiian chain. The terrain of the Big Island is dominated by two volcanic mountains, Mauna Loa and Mauna Kea, both exceeding 4 km in height, well above the typical height of trade-wind inversion (~ 2 km). During the month of August, trade winds blow 92% of the time, the highest frequency throughout the year for the state (Sanderson 1993), because of the presence of the semi-permanent Pacific High located northeast of the island chain.

Prior to HaRP (Hawaiian Rainband Project, 11 July – 24 August, 1990), modeling and observational studies by Smolarkiewicz et al. (1988) and Rasmussen et al. (1989) suggested that the formation of the Hilo cloud band results from the dynamic interaction of the trade winds with the island. They theorize that the low-level winds on the windward side of the island reverse direction under a small (< 1) Froude number (Fr) flow regime as a result of orographic blocking. The Froude number is given by $Fr = U/NH$, where U is the mean wind speed, N is the Brünt-Väisälä frequency, and H is the height of the obstacle. A cloud band forms where dynamically induced reverse flow and the incoming trades converge. Comparing pressure perturbations and surface airflow between the composited 12 strongest ($Fr \sim 0.3$) and 12 weakest ($Fr \sim 0.2$) trade-wind days during HaRP, Chen and Nash (1994) showed that when upstream trades are stronger, the orographically induced high-pressure cell on the windward side (Smolarkiewicz et al. 1988) is higher (0.2-0.5 hPa) with lower pressure in the lee-side wake zone.

Rasmussen and Smolarkiewicz (1993) showed that, in their model, the nocturnal cooling doubles the depth and speed of the reverse flow. However, they maintain that the convergence line offshore is primarily a result of dynamic forcing; the nocturnal cooling has very little effect on the position of the convergence line. However, it is important to note that the effects of

nocturnal cooling are underestimated by their model (Feng and Chen, 2001). In the early morning before sunrise, the virtual temperature differences between the surface air on the windward side and the upstream value at the same altitude reach -4 K (Chen and Wang 1994; Feng and Chen 1998) and are only ~ -1 K in the modeling studies of Smolarkiewicz et al. (1988) and Rasmussen et al. (1989).

Using PAM (Portable Automatic Mesonet) surface data collected during HaRP, Chen and Nash (1994) and Chen and Wang (1994) studied the precipitation, airflow, and thermodynamic fields over the island of Hawaii throughout the diurnal cycle. Chen and Nash (1994) showed that with mean weak winds caused by orographic blocking on the windward side, the thermally driven circulations there become significant. Chen and Wang (1994) found that, on the windward side, the onset of anabatic (katabatic) flow occurs after sunrise (before sunset) on the upper slopes where virtual temperature first becomes warmer (cooler) than environmental values. The timing of the wind shift during these periods can also be affected by rainshowers and cloud cover that modify the thermodynamic fields near the surface (Chen and Wang 1995). Carbone et al. (1995) show that the leading edge of the downslope flow resembles a density current. Throughout the night, the katabatic flow deepens and intensifies, then gradually extends over the ocean (Feng and Chen 1998). The location of the convergence zone between the offshore flow and the incoming trades is related to the offshore extension of the katabatic flow (Feng and Chen 1998) and is not only dependent on Fr as suggested by modeling studies (Smolarkiewicz et al. 1988; Rasmussen and Smolarkiewicz 1993). Rain evaporative cooling serves to deepen the katabatic flow (Wang and Chen 1995). The strength of the upstream trades affects the onset time of the katabatic (anabatic)/offshore (onshore) flow in the late afternoon (early morning). Under

stronger trade winds, offshore flow over the windward side begins later in the evening and ends earlier in the morning (Chen and Nash 1994).

Reisner and Smolarkiewicz (1994) studied low (< 1) Fr flow past a three-dimensional obstacle with uniform heating at the surface and obtained a simple criterion for the transition from the blocked flow to an unblocked flow. Raymond and Rotunno (1989) and Lin et al. (1993) introduced thermal Froude number, U/Nd , where d is the depth of the cooling/heating region, to study flow response forced by prescribed heat sinks when the environment is stably stratified. In the work of Lin et al. (1993), the prescribed cooling region is set at the center of their 2-D model domain with a depth of 3 km. A density current is able to form only when the cooling is strong enough to produce an outflow that spreads faster than the compensating gravity waves. Even though the leading edge of land breezes on the windward side of the island of Hawaii resembles a density current, to study the land/sea-breeze circulations, mountain/valley winds and the secondary circulations forced by land-sea thermally contrast for the island of Hawaii throughout the diurnal cycle requires a 3-D mesoscale model. Furthermore, the results from 2-D simulations may not be applicable to 3-D flows as flow splitting occurs on the windward side of the island of Hawaii owing to the fact that the mountain height are well above the trade-wind inversion (Leopold 1949; Schär and Smith 1993). The incoming flow may be deflected around the obstacle rather than passing through the heat sink as in a 2-D model.

Chen and Feng (2001) use the composite upstream sounding derived from 20 HaRP soundings taken by the NCAR Electra to initialize the Pennsylvania State University-National Center for Atmospheric Research (PSU-NCAR) fifth generation Mesoscale Model (MM5; Dudhia 1993) without considering the diurnal heating cycle. They show that in addition to Fr, the simulated island airflow and cloud distributions are sensitive to trade-wind inversion height

(Chen and Feng 1995) and net diabatic heating rate associated with clouds and precipitation. With nocturnal cooling, Feng and Chen (2001) successfully simulated the major observed features associated with the nocturnal flow regime, including the formation of nocturnal inversion, development and gradual offshore extension and deepening of the katabatic flow, shifting of the overall cloudy area from the windward slopes to the ocean, and generation of clouds within the offshore convergence zone in the early morning. They also simulated the dependence of depth, strength, and offshore extension of the offshore flow on rain evaporation. Recently, the full diurnal cycles of island-scale airflow and weather over the island of Hawaii were successfully simulated by Yang et al. (2005) using MM5 coupled with an advanced land surface model (Chen and Dudhia 2001) with proper treatments of lower boundary conditions over land (Zhang et al. 2005). In their model, the thermally direct diurnal circulation cells on the windward side for both the daytime and night flow regimes are reproduced (Yang et al. 2005; figs. 25 and 26).

HaRP studies reveal that there are three rainfall regimes during the diurnal cycle on the windward side: the nocturnal rainfall regime over the windward lowlands, the early morning coastal rainfall regime, and the daytime orographic rainfall regime (Chen and Nash 1994; Chen and Feng 1995). During the evening hours, rainfall totals are at their maximum (Schroeder et al. 1977) over the windward lowlands as a result of the convergence between the katabatic flow and the moist incoming trade winds *inland* (Chen and Nash 1994; Feng and Chen 1998). The rising motion caused by the low-level convergence is enhanced by orographic lifting aloft (Feng and Chen 2001). With further cooling, the convergence zone and the maximum rainfall axis shift toward the coast as the leading edge of the katabatic flow propagates toward the coast and deepens (Chen and Nash 1994; Feng and Chen 1998). In the early morning, rainbands are

frequently observed offshore in the convergence zone (Leopold 1949; Lavoie 1967; Garrett 1980). The origin of nocturnal and early morning rainfall may be attributed to pre-existing upstream cloud patches (Larson 1978; Austin et al. 1996; Wang and Chen 1998; Wang et al. 2000) that are enhanced by the flow deceleration and the convergence zone (Rasmussen et al. 1993; Carbone et al. 1998; Wang et al., 2000) or to rainshowers that form within the convergence zone (Leopold 1949; Takahashi 1981; Rasmussen et al. 1993; Lee and Chen 1999). In the afternoon hours, orographic clouds develop on the slopes as a result of the development of combined anabatic and sea breeze winds (Leopold 1949; Lavoie 1967; Garrett 1980; Feng and Chen 1998) with relatively clear skies over the ocean. The diurnal rainfall regimes over the island of Hawaii are well simulated by our recent modeling studies (Yang et al. 2005).

The main objective of this study is to improve our understanding of rainfall production on the windward side of the island of Hawaii. We will study the diurnal rainfall variations on the windward side under various trade-wind strengths to investigate the effects of trade-wind strength on the rainfall production for different diurnal rainfall regimes. Rainfall diurnal cycles for the 12 strongest and 12 weakest trade-wind days during the HaRP period, characterized by Chen and Nash (1994) will be analyzed. In addition, we would like to extend our analysis of rainfall diurnal cycle under various trade-wind strengths to the summers of 1997-2000 using the routine rain gauge data and the rainfall data from the newly deployed hydronet over the Hawaiian Islands.

Extending the analysis to 1997-2000 will serve two purposes. The first is to expand the database to more samples in order to further eliminate uncertainties and biases. Secondly, this will help determine whether the rainfall patterns from the HaRP experiment in 1990 are

representative or not. Other features on a synoptic scale that may affect the trade-wind strength over the Hawaiian Islands will be discussed.

2. Data Sources

Data from the 50 NCAR PAM stations during HaRP (Fig. 1) are used. Pressure, temperature, wet-bulb temperature, u - and v -wind components, rainfall and radiation measurements* (from stations 13, 15, and 16) are recorded at one-minute intervals. Surface wind fields are based on 15-minute averages as described in Chen and Nash (1994). Rainfall measurements at each PAM station have a resolution of 0.254 mm. Station 15 contains faulty rainfall data and the data from this station are not used in the analysis.

Out of the 45 HaRP days, the 12 strongest and 12 weakest trade-wind days were determined from wind data at PAM stations from the northernmost (Hawi) and southernmost (South Point) locations by Chen and Nash (1994). Winds averaged 7.8 m s^{-1} for the 12 strongest days, which are July 11, 13, 24, 25, 28 and August 8, 9, 12, 13, 16, 18, 23. The weakest trade-wind days are July 15, 20, 21, 27, 29, 30 and August 3, 5, 7, 19, 20, 21, with an average wind speed of 5.6 m s^{-1} .

The classification of trade-wind strength from the 1990 HaRP wind data is consistent with the NCEP (National Centers for Environmental Prediction)/NCAR's 1990 reanalysis wind data taken from the grid point 20°N , 155°W at the 1000-hPa level, except the wind speed from the NCEP/NCAR reanalysis is slightly lower. The NCEP/NCAR reanalysis may underestimate the wind speed over the open ocean immediately upstream of Hilo (Yang et al. 2005) but still can be used to rank the trade-wind strength during the period. The averaged wind speed and the

*Radiation measurements were only taken at stations 13, 15, and 16.

standard deviations from the 1990 NCEP/NCAR reanalysis wind data for the 12 strong and the 12 weak HaRP days are shown in Table 1. Winds for the strong and weak trade days are significantly different with a confidence level beyond 98% using the Kolmogorov-Smirnov (KS) hypothesis test (Weiss and Hassett, 1991).

Expansion of the dataset to include the period of 11 July - 24 August for years 1997-2000 is made. The NCEP/NCAR reanalysis wind data at 1000-hPa level from the grid-point 20⁰N, 155⁰W are used to rank the trade-wind strength. The years 1999 and 2000 contained significantly stronger trades as compared with HaRP. Days having a positive v -wind component are eliminated. A total of six wind categories are developed for 1997-2000 using the HaRP mean daily wind speeds for the 12 strong ($\overline{u_s}$) and the 12 weak ($\overline{u_w}$) trade-wind days and their standard deviations (σ_s and σ_w) determined from the NCAR/NCEP reanalysis 1000-hPa wind data at the same grid point as references (Table 2). The weakest trade-wind days are those with a mean daily wind speed less than $\overline{u_w} - \sigma_w$. The weak trade-wind days are those with a mean daily wind speed between $\overline{u_w} - \sigma_w$ and $\overline{u_w} + \sigma_w$. Moderate trade-wind days are those having a mean daily wind speed ranging from $\overline{u_w} + \sigma_w$ to $\overline{u_s} - \sigma_s$. The strong trade-wind days are those with a mean daily wind speed between $\overline{u_s} - \sigma_s$ and $\overline{u_s} + \sigma_s$. The moderately strong trade-wind days are those having a mean daily wind speed from $\overline{u_s} + \sigma_s$ to $\overline{u_s} + 2\sigma_s$. The very strong trade-wind days are those having a mean daily wind speed greater than $\overline{u_s} + 2\sigma_s$. The KS significance test results show that the winds in different trade-wind regimes differ significantly with a confidence level beyond 98%.

For the very strong trade-wind regime, the semi-permanent subtropical high (~1026 hPa) to the north of the island chain dominates the synoptic map, which features relatively large

pressure gradients over the Hawaiian Islands (Fig. 2a). In contrast, the weakest trade-wind composite map (Fig. 2b) shows weaker pressure gradients because the high pressure cell is split by the passage of a mid-latitude cold front farther to the north. Chen and Feng (1995) have shown that for the 20 July 1990 case, a mid-latitude storm passes farther to the north of the island chain and splits the subtropical high.

Average inversion base heights from Hilo soundings for different trade-wind regimes ranged between 789 hPa and 808 hPa, except for the weakest trade regime which had a lower average inversion height of 827 hPa (Table 3). The geopotential height for the weakest trade regime was slightly higher (Fig. 2b) because the ridge axis of the subtropical high is pushed slightly southward during the passage of a mid-latitude storm.

The rainfall data from eighteen National Weather Service (NWS) Honolulu Forecast Office (HFO) hydronet stations over the island of Hawaii (Table 4 and Fig. 3a) during the period of 11 July - 24 August for years 1997-2000 are used. Rainfall data from these stations are measured by a telemetered tipping bucket rain gauge. This real-time rain gauge network collects data at 15-minute intervals with a resolution of 0.254 mm (0.01 in.). Many gauges are located in remote locations throughout the State of Hawaii and data quality is variable. For some periods, 15-minute interval data were not available. The data provided are given in running totals, so when rainfall reaches 99.99 inches, it will be automatically reset to 0 inches. Individual counters are manually reset, denoted with the letter “m”, if any work or maintenance is performed on that particular gauge, regardless of the reading at that time.

The National Climatic Data Center (NCDC) rainfall data for the island of Hawaii (Table 5) will be added to the NWS Hydronet data. There are nineteen NCDC stations (Fig. 3b)

measuring hourly precipitation with a resolution of a 2.54 mm (0.1 in.). The only exceptions come from Hilo Airport and Lihue Airport where the resolution is 0.254 mm (0.01 in.).

3. Transect from the Upper Slope to the Coast

A transect from the upper slopes to the coastline west of Hilo is constructed from data collected from PAM stations located at Kulani Prison (Station 11, elevation 1579 m), North Kulani Road (Station 10, elevation 506 m), Hawaiian Acres (Station 4, elevation 202 m), and Paradise Park (Station 8, elevation 17 m) during HaRP to show the diurnal cycles of rainfall and averaged surface winds (Fig. 4).

For both the 12 strong and 12 weak trade-wind days during HaRP, the surface airflow along the transect is dominated by the daytime upslope-onshore flow and nighttime katabatic-offshore flow (Figs. 5a and 6a). Note that for the strong trade-wind regime, the nighttime katabatic flows at stations 10 and 11 have a more northerly component compared to the weak trade-wind regime. For weak trade-wind days (Fig. 6a), the daytime upslope flow has a more easterly wind component compared to strong trade-wind days (Fig. 5a). Chen and Nash (1994) found that the u -component difference, $u_{\text{strong}} - u_{\text{weak}}$, between the strong and weak trade-wind days showed a small positive difference ($> 1 \text{ m s}^{-1}$) on the windward slopes for both the daytime and nighttime flow regimes. The difference indicates that the upslope flow during the day is slightly weaker and the nighttime katabatic flow slightly stronger for the strong than the weak trade-wind days, consistent with the observed higher pressure deviations on the windward side when trades are stronger (Chen and Nash 1994).

Both the strong and weak trade regimes display an evening rainfall regime after sunset (Figs. 5b and 6b). However, the nocturnal rainfall on the windward lower slopes is more frequent with a higher rain rate for strong trade-wind days (1.2 m h^{-1}) (Fig. 5b) than weak trade-

wind days (Fig. 6b). The maximum hourly nocturnal rainfall frequency exceeds 60% under strong trades (Fig. 5c). In comparison, the precipitation is less frequent at night for weak trade-wind days (40%) (Fig. 6c) with lower mean rain rates ($0.4 - 0.8 \text{ mm h}^{-1}$), except a local rainfall maximum (1.2 mm h^{-1}) during 0200-0300 HST over the coast (Fig. 6b). Some of the nocturnal rainshowers originated far upstream and were enhanced by flow deceleration upstream, the convergence between the katabatic flow and the incoming trade-wind flow, and orographic lifting aloft (Carbone et al. 1998; Frye and Chen 2001). In some cases, trade-wind showers were generated within the leading edge of the katabatic flow (Lee and Chen 1999). Modeling studies (Feng and Chen 2001; Yang et al. 2005; Yang and Chen 2007) show that at night, the thermally driven circulation cell on the windward side is characterized by descending airflow immediately above the slope surface, a convergence zone between the decelerating incoming trade-wind flow and the katabatic flow, and rising motion aloft due to orographic lifting. It appears that the rising motions caused by the convergence between decelerating incoming trades and the katabatic flow west of Hilo, and the orographic lifting aloft (Chen and Nash 1994) are more significant when trades are stronger, resulting in higher nocturnal rainfall there. Recent modeling work by Yang and Chen (2007) suggests that neither dynamic forcing (without land surface forcing) (Smolarkiewicz et al. 1988) nor land surface forcing (without terrain) alone is adequate to account for the rainfall production on the windward side. From their model sensitivity tests with different terrain heights, they show that the rainfall production on the windward side in the model is negatively correlated with variations in Froude number due to differences in model terrain heights. The rainfall production on the windward side is closely related to rising motions caused by nonlinear interactions among orographic lifting, orographic blocking, land surface processes and feedback effects from convection.

For both strong and weak trade-wind days, as the katabatic flow extends toward the coast throughout the night, the rainfall rates on the windward lowlands decrease. For both regimes, rainfall frequency along the windward coastal region and over the windward lowlands is relatively high (30-60%) before sunrise. Modeling studies (Feng and Chen 2001; Yang et al. 2005) show that the simulated flow deceleration of the incoming trade-wind flow on the windward side is most significant in the early morning when the katabatic flow is the deepest with a maximum horizontal extent (Chen and Feng 1998) in agreement with aircraft observations (Esteban 2002). The early morning rainfall along the coast is frequently related to pre-existing trade-wind rainshowers upstream that are enhanced within the offshore convergence zone as they move toward the island of Hawaii (Austin et al. 1996; Wang and Chen 1998; Wang et al. 2000). These rainshowers weaken and dissipate as they move over the cooler and drier offshore flow (Wang and Chen 1998).

In contrast to the nocturnal flow regime, daytime (0800-1600 HST) rainfall amounts are slightly lower (Fig. 5b) with lower rainfall frequencies ($\sim 20\%$) (Fig. 5c) when trades are stronger. This is consistent with a slightly weaker upslope flow for strong trade-wind days as compared to weak trade-wind days (Chen and Nash 1994). A local rainfall maximum ($0.8\text{-}1.6 \text{ mm h}^{-1}$) during the same time period occurs over the upper slopes under weak trades with higher rainfall frequencies ($\sim 40\%$) (Fig. 6c). Under weak trades, the daytime rainfall starts on the windward lowlands at Hawaiian Acres (Station 4, elevation 202 m) in the morning (Fig. 6b). Rainfall increases to more than 1.2 mm h^{-1} a few hours later at the lower slopes at North Kulani Road (Station 10) (Fig. 6b) as a result of the establishment of upslope flow (Fig. 6a). The greatest intensity occurs at station 10 in the late afternoon hours for weak trade-wind days with hourly rainfall frequencies $> 40\%$. The trade-wind inversion height is another factor that affects

the rainfall production on the windward side. Feng and Chen (1995) show that for higher trade-wind days, the afternoon orographic clouds are closer to the summits and more extensive with higher rainfall amounts. The mean trade-wind inversion height is slightly higher for the weak trade-wind days (762 hPa) than for the strong trade-wind days (778 hPa) (Table 3). However, the difference in trade-wind inversion height between the strong and weak trade-wind days during HaRP is relatively small. During the summers of 1997-2000, the mean trade-wind inversion height is the lowest (827 hPa), when the trade-wind strength is the weakest (Table 3). The impact of trade-wind strength on daytime rainfall on the windward side will be investigated further in the next section.

The above results show that the effects of trade-wind speed upon windward rainfall production vary throughout the diurnal cycle. Nocturnal rainfall amounts are higher with more frequent trade-wind showers when trades are stronger because the convergence between the decelerating incoming trades and the katabatic flow and the orographic lifting aloft (Chen and Nash 1994; Yang and Chen 2007) are more significant when trades are stronger. In the afternoon hours, orographic showers over land are more frequent with slightly higher rain rates for weak trade-wind days than strong trade-wind days. However, with relatively small sample sizes during HaRP, we would like to extend our analyses to the summers of 1997-2000.

4. Extending HaRP Analysis

Having only 12 strong and 12 weak composite days to work with from the 1990 HaRP experiment, we extended our analyses with a larger database to provide more convincing evidence of the impact of trade-wind speed on rainfall production during the diurnal cycle on the windward side. Evolution of rainfall patterns during the diurnal cycle under different trade-wind

strength for the summer of 1997-2000 based on NCDC (National Climate Data Center) and hydronet data will be examined in this section.

Daily rainfall totals indicate that stronger trade winds correspond to higher rainfall amounts on the windward slopes of the island of Hawaii as the moisture laden trade-wind flow is lifted over the windward slopes. The daily rain rate totals show a maximum over the windward lowlands at 4 mm day^{-1} (Fig. 7a) for weak trade days, 8 mm day^{-1} for moderate trade days (Fig. 7b), 6 mm day^{-1} for strong trade days (Fig. 7c), 12 mm day^{-1} for moderately strong trade days (Fig. 7d), and a dramatic 20 mm day^{-1} for very strong trade days (Fig. 7e). The daily rainfall totals are greater when trades are stronger. These results are consistent with Carbone et al. (1998) and Tuttle et al (2002). In addition to daily rainfall totals, we will investigate the impact of trade-wind strength on rainfall distribution and amounts for different diurnal rainfall regimes.

Around midnight (2300-0300 HST), a northwest-southeast rainfall axis of 1.0 mm h^{-1} exists over the windward lowlands and the coast for very strong trade-wind days (Fig. 8a). In comparison, weak trade-wind days display a rainfall maximum rate of only 0.2 mm h^{-1} (Fig. 8b) located closer to the coastline. As suggested by Frye and Chen (2001) in a case study, the convergence between the katabatic winds and incoming decelerating trade-wind flow and the orographic lifting aloft are more pronounced under stronger trades, evidenced by having a rainfall axis with rain rates five times greater (Fig. 8a) than that of the weak trade-wind days (Fig. 8b).

The period before sunrise (0300-0700 HST) also displays a large disparity in rainfall rates. Similar to a strong ($\sim 11 \text{ m s}^{-1}$) trade-wind case (Frye and Chen 2001), the maximum rainfall axis remains over land for the very strong trade wind regime (Fig. 9a). Rainfall rates (1.2 mm h^{-1}) near the coast to the northwest of the Hilo Bay area (Fig. 9a) indicate that the

convergence is stronger under stronger trade conditions, thereby resulting in more rainfall. Precipitation for the weak trades (Fig. 9b) shows a lower rainfall rate and a shifting of the maximum rainfall axis farther out toward the coastal region. It is apparent that under weaker trade-wind conditions, the thermally induced katabatic flow extends farther offshore (Feng and Chen 1998).

In the morning (0700-1100 HST), the axis of the rainfall maximum for the very strong trade-wind category remains over the windward lowlands west of Hilo (Fig. 10a). With weak trades, the axis is located farther eastward toward the eastern tip of the island of Hawaii (Fig. 10b) showing the least amount of rainfall over land under this trade-wind regime. These results are attributed to the fact that the katabatic flow is more pronounced under weaker trade-wind conditions (Chan and Nash 1994; Feng and Chen 1998). Note that at 0900 HST, the splitting airflow in the Hilo Bay area has an onshore wind component for strong trade-wind days during HaRP, whereas for weak trade wind days, it still has an offshore component at this time (Chen and Nash 1994; fig. 16c).

The period around noontime (1100-1500 HST) is characterized by the development of upslope flow. For very strong trade winds, the rainfall axis has shifted from the lowlands in the early morning to slightly higher elevation (Fig. 11a). With weak trade winds, rainfall rates over the windward lower slopes gradually increase as a result of the development of orographic clouds and showers (Fig. 11b). The afternoon period until sunset (1500-1900 HST) reveals that under very strong trades, a rainfall axis of 0.6 mm h^{-1} exists over the windward lowlands (Fig. 12a). Under the weak trade-wind regime, rainfall rates over the lower windward slopes west of Hilo (Fig. 12b) are higher than earlier due to orographic lifting provided by the combined anabatic/trade-wind flow along the windward slopes. During HaRP orographic rainshowers on

the windward slopes (Station 11, elevation 1579 m) in the afternoon hours are more frequent (~40%) for weak trades (Fig. 6c) than strong trades (Fig. 5c). Since there are no NCDC or Hydronet stations located above the 1000-m terrain contour west of Hilo (Fig. 3), the maximum rainfall axis may be located at a higher elevation, similar to the situation for weak trade-wind conditions during HaRP (Fig. 6b). Under weak trades, the diurnal rainfall variations have pronounced afternoon maxima on the windward slopes.

For very strong trade-wind days, the rainfall rates over the windward lowlands in the early evening (1900-2300 HST) (Fig. 13 a) are higher than in the later afternoon hours (Fig. 12a). The rainfall axis of 0.8 mm h^{-1} remains over the windward lowlands and extends to the west of the Hilo Bay area. For weak trade winds, there is a rapid decrease of rainfall on the windward slopes after sunset (Fig. 13b) as the daytime upslope wind is replaced by nighttime katabatic flow. Under stronger trades, in addition to upstream flow deceleration, focusing and enhancement of trade-wind showers in the convergence zone during the evening transition with a well-defined rainfall axis in the windward lowlands (Fig. 13a) (Frye and Chen 2001) is more pronounced. These results are consistent with those presented in Section 3 using a limited sample size during HaRP. The nocturnal rainfall is significantly higher and farther inland when trades are stronger. On the other hand, weak trade-wind days have a pronounced diurnal rainfall maximum on the windward slopes in the late afternoon hours. Throughout the diurnal cycle, rainfall amounts on the windward side are statistically higher with more frequent rainshowers under stronger trades, except in the late afternoon hours.

The daily rainfall totals show a maximum along the Kona lee-side coast at 2 mm day^{-1} (Fig. 7a) for weak trade days, 4 mm day^{-1} for moderate trade days (Fig. 7b), 6 mm day^{-1} for strong trade days (Fig. 7c), 8 mm day^{-1} for moderately strong trade days (Fig. 7d), and 12 mm

day⁻¹ for very strong trade days (Fig. 7e). These results are consistent with Yang and Chen (2003) (their fig. 18). The rainfall along the Kona coast has an early evening maximum (Chen and Nash 2004; Yang and Chen 2003). Yang and Chen (2003) and Yang and Chen (2007) suggest that the evening rainfall maximum there is caused by the convergence between the land breezes and the dynamically induced westerly flow between the two counter-rotating vortices in the lee (Smith and Grubišić, 1993). The westerly flow offshore and the convergence along the coast are expected to be more pronounced when trades are stronger (Yang and Chen 2003).

5. Summary

Rainfall rates on the windward side, except in the late afternoon hours, are statistically higher throughout the diurnal cycle when trades are stronger. The thermally driven diurnal winds distinctly affect the timing and location of rainfall occurrences under different trade-wind strength. For normal or strong trade-wind regimes, the rainfall distribution has a nocturnal maximum on the windward lowlands west of Hilo caused by the convergence of the katabatic flow and the incoming decelerating trade-wind flow, and orographic lifting aloft. The maximum rainfall axis shifts farther inland when trades are stronger.

For the weak ($\leq 5 \text{ m s}^{-1}$) trade-wind regime, the rainfall distribution has a late afternoon maximum on the windward slopes as a result of the development of anabatic winds. In the afternoon hours, the thermally driven anabatic winds are more significant when trades are weaker. At night, under weaker trades, in addition to weaker orographic lifting aloft, the convergence between the katabatic/offshore flow and the weaker incoming trade-wind flow occurs farther eastward toward the coast and extends farther offshore in the early morning. As a result, after midnight and in the early morning, rainfall is lower and the maximum rainfall axis is displaced farther eastward toward the coast when trades are weaker.

REFERENCES

- Austin, G. R., R. M. Rauber, H. T. Ochs III, and L. J. Miller, 1996: Trade-wind clouds and Hawaiian rainbands. *Mon. Wea. Rev.*, **124**, 2126-2151.
- Carbone, R. E., W. A. Cooper, W.-C. Lee, 1995: Forcing of flow reversal along the windward slopes of Hawaii. *Mon. Wea. Rev.*, **123**, 3466-3480.
- _____, J. D. Tuttle, W. A. Cooper, V. Grubišić, W. C. Lee, 1998: Trade-wind rainfall near the windward coast of Hawaii. *Mon. Wea. Rev.*, **126**, 2847-2863.
- Chen, F., and J. Dudhia, 2001: Coupling an advanced land surface-hydrology model with the Penn State-NCAR MM5 modeling system. Part I: Model Implementation and Sensitivity. *Mon. Wea. Rev.*, **129**, 569–585.
- Chen, Y.-L., and J. Feng, 2001: Numerical simulations of airflow and cloud distributions over the windward side of the island of Hawaii. Part I: The effects of trade wind inversion, *Mon. Wea. Rev.*, **129**, 1117-1134.
- _____, and _____, 1995: The influences of inversion height on precipitation and airflow over the Island of Hawaii. *Mon. Wea. Rev.*, **123**, 1660-1676.
- _____, and J. J. Wang, 1995: The effects of precipitation on the surface temperature and airflow over the island of Hawaii. *Mon. Wea. Rev.*, **123**, 681-694.
- _____, and _____, 1994: Diurnal variations of surface thermodynamic fields on the island of Hawaii. *Mon. Wea. Rev.*, **122**, 2125-2138.
- _____, and A. J. Nash, 1994: Diurnal variations of surface airflow and rainfall frequencies on the island of Hawaii. *Mon. Wea. Rev.*, **122**, 34-56.

- Dudhia, J. 1993: A nonhydrostatic version of the Penn state-NCAR mesoscale model: validation tests and simulation of an Atlantic cyclone and cold front. *Mon. Wea. Rev.*, **121**, 1493-1513.
- Esteban, M. A., 2002: Impact of trade-wind strength on precipitation and circulation of the island of Hawaii. MS Thesis, Department of Meteorology, University of Hawaii, Honolulu, HI 96822.
- Feng, J., and Y.-L. Chen, 1998: Evolution of katabatic flow on the Island of Hawaii on 10 August 1990. *Mon. Wea. Rev.* **126**, 2185-2199.
- _____, and _____, 2001: Numerical simulations of airflow and cloud distributions over the windward side of the island of Hawaii. Part II: Nocturnal flow regime. *Mon. Wea. Rev.*, **129**, 1135-1147.
- Frye, J. L., and Y.-L. Chen, 2001: Evolution of downslope flow under strong opposing trade-winds and frequent trade-wind rainshowers over the Island of Hawaii. *Mon. Wea. Rev.*, **129**, 956-977.
- Garrett, A. J., 1980: Orographic cloud over the eastern slopes of Mauna Loa Volcano, Hawaii, related to insolation and wind. *Mon. Wea. Rev.*, **108**, 931-941.
- Larson, R. N., 1978: Summer trade-wind rainfall in the Hawaiian Islands. M.S. Thesis, Department of Meteorology, University of Hawaii, 84 pp.
- Lavoie, R. L., 1967: Air motions over the windward coast of the Island of Hawaii. *Tellus*, **19**, 354-358.
- Leopold, L. B., 1949: The interaction of trade-wind and sea breeze, Hawaii. *J. Meteor.*, **8**, 533-541.

- Li, J., and Y.-L. Chen, 1999: A case study of nocturnal rain showers over the windward coastal region of the Island of Hawaii. *Mon. Wea. Rev.*, **127**, 2674-2692.
- Lin, Y.-L., T.-A. Wang, and R. P. Weglarz, 1993: Interactions between gravity waves and cold air outflows in a stably stratified uniform flow. *J. Atmos. Sci.*, **50**, 3790-3816.
- Rasmussen, R. M, and P. K. Smolarkiewicz, 1993: On the dynamics of Hawaiian cloud Bands. Part III: Local aspects. *J. Atmos. Sci.*, **50**, 1560-1572.
- _____, _____, and J. Warner, 1989: On the dynamics of Hawaiian cloud bands: Comparison of model Results with observations and island climatology. *J. Atmos. Sci.*, **46**, 1589-1608.
- Raymond, D. and R. Rotunno, 1989: Response of a stably stratified to cooling. *J. Atmos. Sci.*, **46**, 2830-2837.
- Sanderson, M., Ed., 1993. *Prevailing Trade-winds, Weather and Climate in Hawaii*. University of Hawaii Press, 126pp.
- Schär, C., and R. B. Smith, 1993: Shallow-water flow past isolated topography. Part I: Vorticity production and wake formation. *J. Atmos. Sci.*, **50**, 1373–1400.
- Schroeder, T. A., B. J. Kilonsky, and B. N. Meisner, 1977: Diurnal variation in rainfall and cloudiness. UHMET Rep. 77-03, 67 pp. [Available from Department of Meteorology, University of Hawaii, Honolulu, HI 96822.]
- Smith, R. B., and V. Grubišić, 1993: Aerial observation of Hawaii's wake, *J. Atmos. Sci.*, **50**, 3728-3750.
- Smolarkiewicz, P., R. M. Rasmussen, T. L. Clark, 1988: On the dynamics of Hawaiian cloud bands: Island forcing. *J. Atmos. Sci.*, **45**, 1872-1905.
- Takahashi, T., 1981: Warm rain study in Hawaii – Rain initiation. *J. Atmos. Sci.*, **38**, 347-369.

- Tuttle, J. D., R. E. Carbone, and J. J. Wang, 2000: Trade-wind rainfall near the windward coast of Hawaii: Corrected data yield improved results. *Mon. Wea. Rev.* **128**, 896-900.
- Wang, J.-J., R. M. Rauber, H. T. Ochs III, R. E. Carbone, 2000: The effects of the island of Hawaii on offshore rainband evolution. *Mon. Wea. Rev.* **128**, 1052-1069.
- _____, and Y.-L. Chen, 1998: A case study of trade-wind rainbands and their interaction with the island-induced airflow. *Mon. Wea. Rev.* **126**, 409-423.
- _____, and _____, 1995: Characteristics of near-surface winds and thermal profiles on the windward slopes of the Island of Hawaii. *Mon. Wea. Rev.* **123**, 3481-3501.
- Weiss, N.A., and M. J. Hassett, 1991: Introductory Statistics. *Addison-Wesley Publishing Co.*, 960 pages.
- Yang, Y., and Y.-L. Chen, 2007: Effects of terrain heights and sizes on island-scale circulations and rainfall. *Mon. Wea. Rev.*, (In Press).
- _____, _____, and F. M. Fujioka, 2005: Numerical simulations of the island induced circulations for the island of Hawaii during HaRP. *Mon. Wea. Rev.*, **133**, 3693-3713.
- _____, and _____, 2003: Circulations and rainfall on the leeward side of the island of Hawaii during HaRP. *Mon. Wea. Rev.*, **131**, 2525-2542.
- Zhang, Y., Y. L. Chen, S. Y. Hong, H. M. H. Juang and K. Kodama, 2005: Validation of the coupled NCEP Mesoscale Spectral Model and an advanced Land Surface Model over the Hawaiian Islands: Part I: Summer trade-wind conditions over Oahu and heavy rainfall events. *Wea. Forecasting*, **20**, 847-872.

TABLE CAPTIONS

- Table 1. Listing of different wind categories with respective speed range based on the mean and standard deviation winds (m s^{-1}) from HaRP, mean winds, estimated Froude numbers and number of days.
- Table 2. Dates used for NCEP/NCAR reanalysis wind data for each year from 1997-2000 under each wind category.
- Table 3. Mean and standard deviation of inversion base heights under different trade-wind regimes.
- Table 4. National Weather Service hydronet stations over the island of Hawaii.
- Table 5. National Climatic Data Center rainfall stations over the island of Hawaii.

FIGURE CAPTIONS

- Figure 1. Locations of PAM stations during HaRP.
- Figure 2a. Composite sea-level pressure (hPa) and winds (m s^{-1}) for very strong trade-wind days during 1997-2000.
- Figure 2b. Same as Figure 2a but for the weakest trade-wind days during 1997-2000.
- Figure 3a. Locations of National Weather Service Hydronet Stations.
- Figure 3b. Locations of National Climatic Data Center Stations.
- Figure 4a. Averaged winds and virtual temperature perturbation (ΔT_v) every 1 K between upstream and PAM data for transect from upper slopes to the coast of 45 HaRP days. Winds with one pennant, full barb, and half barb represent 5.0, 1.0, and 0.5 m s^{-1} respectively.
- Figure 4b. Rainfall rate every 0.4 mm h^{-1} for transect of windward coastal PAM stations of 45 HaRP days.
- Figure 5a. Same as Figure 4a but for 12 strong trade-wind days.
- Figure 5b. Same as Figure 4b but for 12 strong trade-wind days.
- Figure 5c. Rainfall incidence (%) of strong trade-wind days. Contour intervals every 20%.
- Figure 6a. Same as Figure 4a but for 12 weak trade-wind days.
- Figure 6b. Same as Figure 4b but for 12 weak trade-wind days.
- Figure 6c. Same as Figure 5c but for 12 weak trade-wind days.
- Figure 7a. Daily rainfall totals (mm day^{-1}) for weak trade-wind days. Terrain contours every 1 km.
- Figure 7b. Daily rainfall totals (mm day^{-1}) for moderate trade-wind days. Terrain contours every 1 km.
- Figure 7c. Daily rainfall totals (mm day^{-1}) for strong trade-wind days.
- Figure 7d. Daily rainfall totals (mm day^{-1}) for moderately strong trade-wind days.
- Figure 7e. Daily rainfall totals (mm day^{-1}) for very strong trade-wind days.
- Figure 8. The rainfall rate (mm h^{-1}) for midnight (2300-0300 HST) for a) very Strong, and b) weak trade-wind regimes in 1997-2000.
- Figure 9. Same as Figure 8 but for 0300-0700 HST.
- Figure 10. Same as Figure 8 but for 0700-1100 HST.

Figure 11. Same as Figure 8 but for 1100-1500 HST.

Figure 12. Same as Figure 8 but for 1500-1900 HST.

Figure 13. Same as Figure 8 but for 1900-2300 HST.

Table 1. Listing of different wind categories with respective speed range based on the mean and standard deviation winds (m s^{-1}) from HaRP, mean winds, estimated Froude numbers and number of days.

Wind Category	Speed (m s^{-1})	Mean wind (\hat{u})	Froude number	Number of Days
HaRP Strong	6.8	6.7	0.27	12
HaRP Weak	5.3	5.2	0.21	12
Very Strong	>8.2	8.9	>0.3	39
Moderately Strong	7.5-8.2	7.8	~0.3	33
Strong	6.1-7.5	6.8	~0.3	53
Moderate	5.6-6.1	5.9	~0.2	17
Weak	4.8-5.6	5.2	~0.2	20
Weakest	<4.8	3.9	<0.2	11

Table 2. Dates used for NCEP/NCAR reanalysis wind data for each year from 1997-2000 under each wind category.

NCEP/NCAR Reanalysis Wind Data							
Very Strong Days				Moderately Strong Days			
1997	1998	1999	2000	1997	1998	1999	2000
0723	0712	0711	0715	0716	0728	0713	0712
0801	0713	0712	0717	0718	0803	0716	0716
0802	0714	0721	0718	0722	0819	0720	0719
	0722	0722	0725	0724		0723	0720
	0723	0726	0726	0730		0725	0724
	0804	0727	0818	0731		0807	0804
	0805	0728	0819	0803		0822	0805
	0820	0729	0820	0806		0824	0806
	0821	0804	0821	0823			0808
	0822	0805	0822				0809
	0823	0806	0823				0810
	0824	0813	0824				0811
							0817
Strong Days				Moderate Days			
1997	1998	1999	2000	1997	1998	1999	2000
0711	0711	0714	0711	0725	0719	0809	0731
0712	0715	0715	0713	0726	0724	0811	0813
0717	0716	0717	0714	0727	0726		
0721	0717	0718	0721	0808	0730		
0729	0718	0719	0722	0809	0815		
0804	0721	0724	0723	0810			
0805	0727	0730	0727	0815			
0807	0729	0803	0728	0821			
0820	0806	0808	0729				
0822	0807	0812	0730				
0824	0813	0818	0801				
	0814	0819	0802				
	0818	0821	0803				
			0807				
			0812				
			0816				

Weak Days

1997	1998	1999	2000
0715	0720	0731	0814
0719	0725	0802	0815
0720	0731	0810	
0728	0802	0820	
0811	0812		
0814	0816		
0816			
0819			

Weakest Days

1997	1998	1999	2000
0713	0801		
0714	0808		
0812	0809		
0813	0810		
0817	0811		
	0817		

Table 3. Mean and standard deviation of inversion base heights (hPa) under different trade wind regimes.

Inversion Base Height (hPa)		
Trade Wind Regimes	Mean	St. Dev.
1990 Strong	779	61.1
1990 Weak	762	57.6
Very Strong	789	50.1
Moderately Strong	790	45.2
Strong	802	52.6
Moderate	793	48.8
Weak	808	47.8
Weakest	828	50.7

Table 4. National Weather Service hydronet stations over the island of Hawaii.

COOPID	Hydronet Station Name	Latitude (°N)	Longitude (°W)	Elevation (m)
80	Laupahoehoe	19.983	155.233	109.7
81	Mountain View	19.550	155.167	466.3
82	Waiaha	19.633	155.950	469.4
83	Pahoa	19.550	155.983	149.5
84	Kealakekua	19.517	155.917	536.4
85	Pahala	19.200	155.483	256.0
86	Kamuela	20.050	155.650	877.8
87	Honokaa	20.067	155.467	387.1
88	Upolu AP	20.267	155.867	29.3
90	Waikii	19.864	155.654	1414.3
91	Piihonua	18.717	155.133	262.1
92	Waiakea Uka	19.667	155.133	304.8
94	Glenwood	19.517	155.167	798.6
95	Honaunau	19.467	155.883	414.6
96	Kahua Ranch	20.133	155.800	987.6
97	Kamuela Upper	20.033	155.667	926.6
98	Hilo	19.717	155.050	2.7
99	Kapapala Ranch	19.283	155.450	652.3

Table 5. National Climatic Data Center rainfall stations over the island of Hawaii.

COOPID	NCDC Station Name	Latitude (°N)	Longitude (°W)	Elevation (m)
511303	Hawaii Volcanoes National Park HQ	19.433	155.267	1210.4
511339	Hawi	19.550	155.833	176.8
511385	Hawaiian Ocean View Estate	19.117	155.783	883.9
511492	Hilo	19.717	155.050	9.1
512156	Huehue	19.750	155.967	597.4
512595	Kahuna Falls	19.867	155.150	371.9
512600	Kahua Ranch HQ	20.133	155.800	987.6
513072	Kamuela	20.050	155.650	877.8
513510	Kaumana	19.683	155.150	359.7
513925	Keaiwa Camp	19.233	155.483	518.2
513987	Kealakekua 4	19.517	155.917	432.8
514098	Keanakolu Camp	19.917	155.350	1609.3
515260	Lalamilo F O	20.017	155.683	797.1
515427	Laupahoehoe	19.983	155.233	115.8
516546	Mountain View #3	19.533	155.133	583.7
517209	Paauhau Mauka	20.067	155.450	341.4
517465	Pahoa School Site	19.500	155.950	208.2
518063	Pohakuloa	19.750	155.533	1984.6
518555	Puu Waa	19.783	155.850	768.1

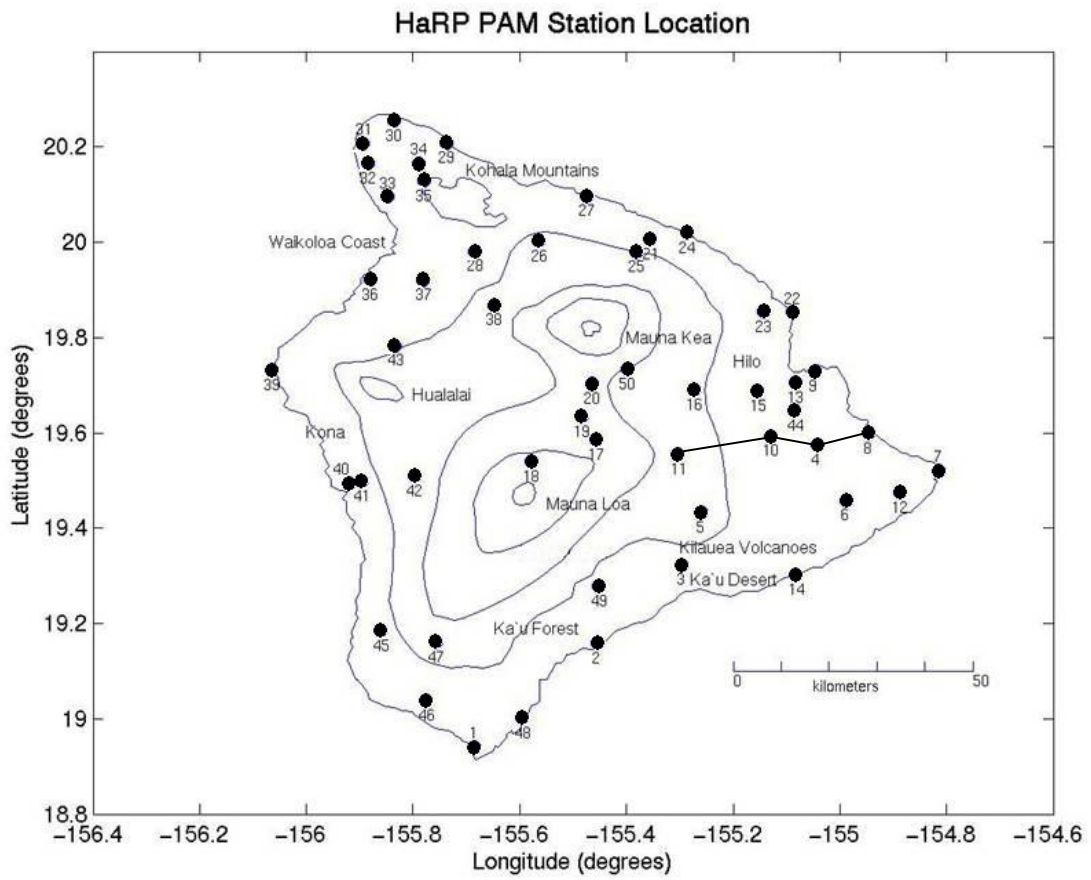


Figure 1. Locations of PAM stations during HaRP.

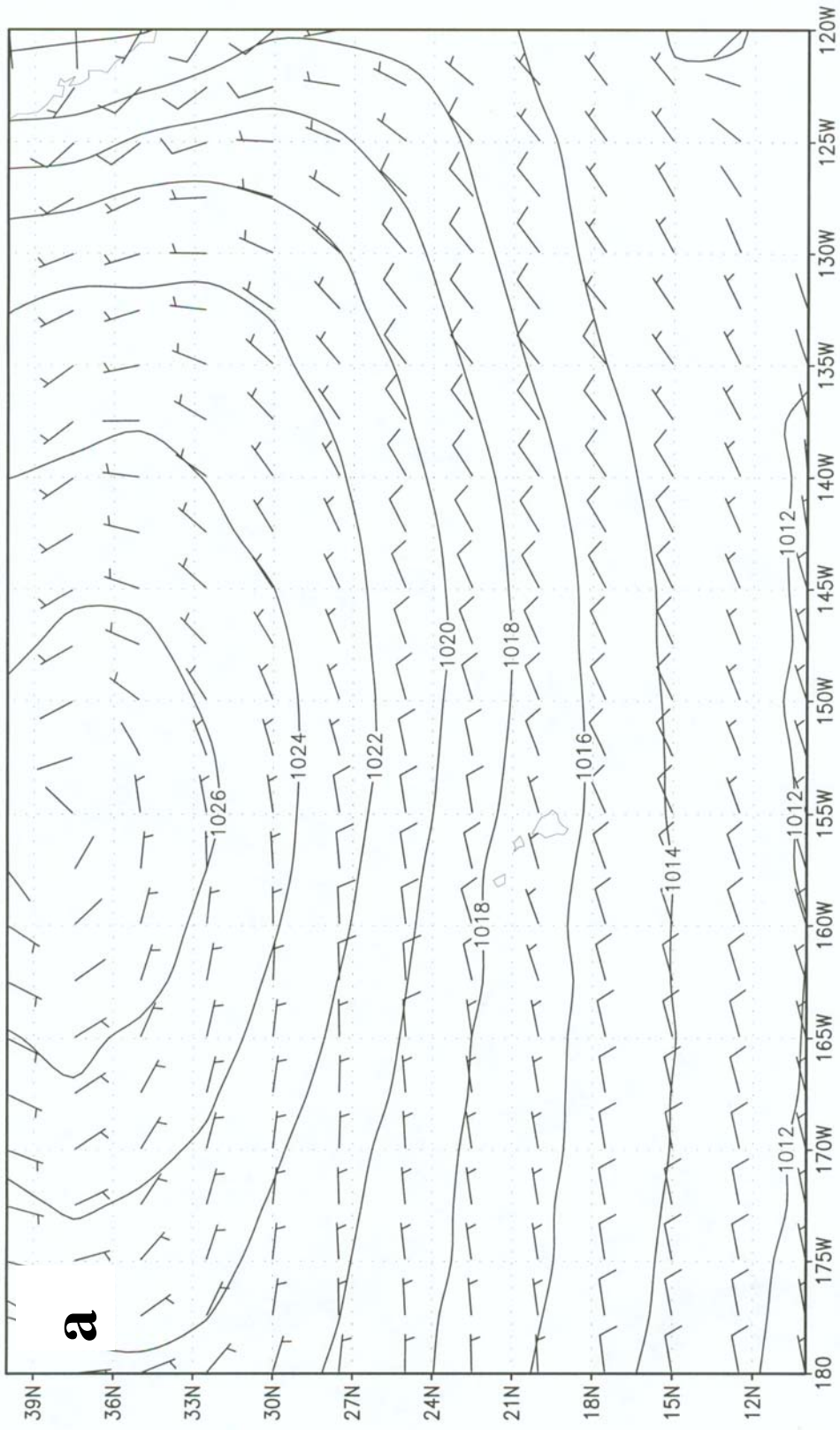


Figure 2a. Composite sea level pressure (hPa) and winds (m s^{-1}) for very strong trade winds during 1997-2000.

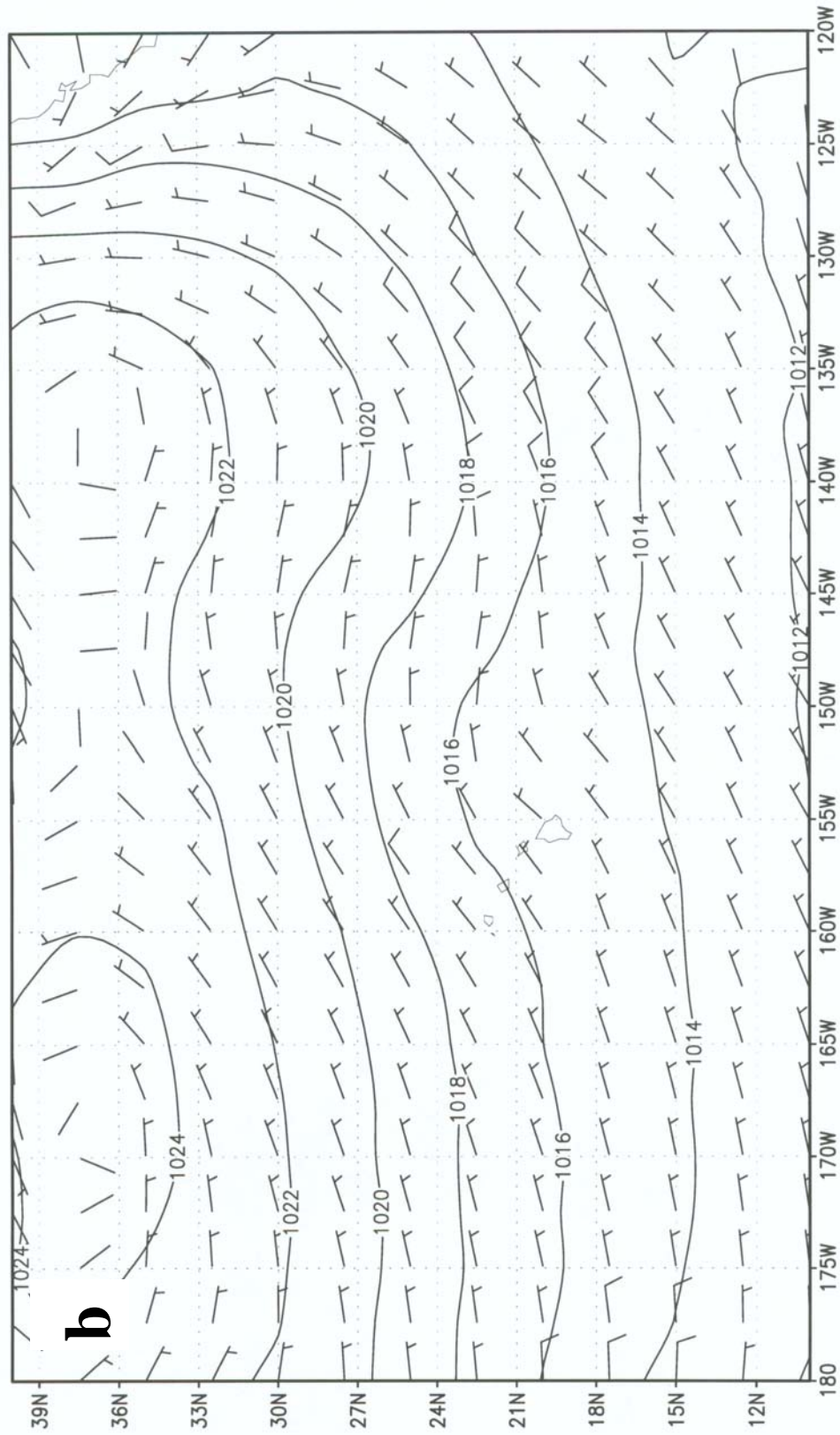


Figure 2b. Composite sea level pressure (hPa) and winds (m s^{-1}) for weakest trade winds during 1997-2000.

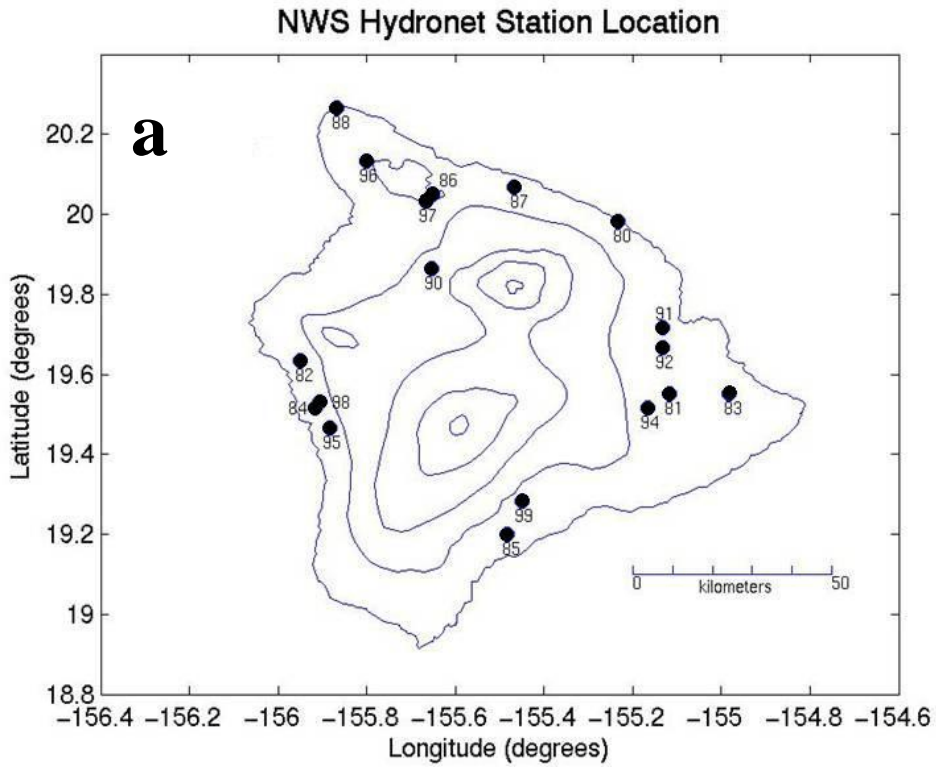


Figure 3a. Locations of National Weather Service hydronet stations.

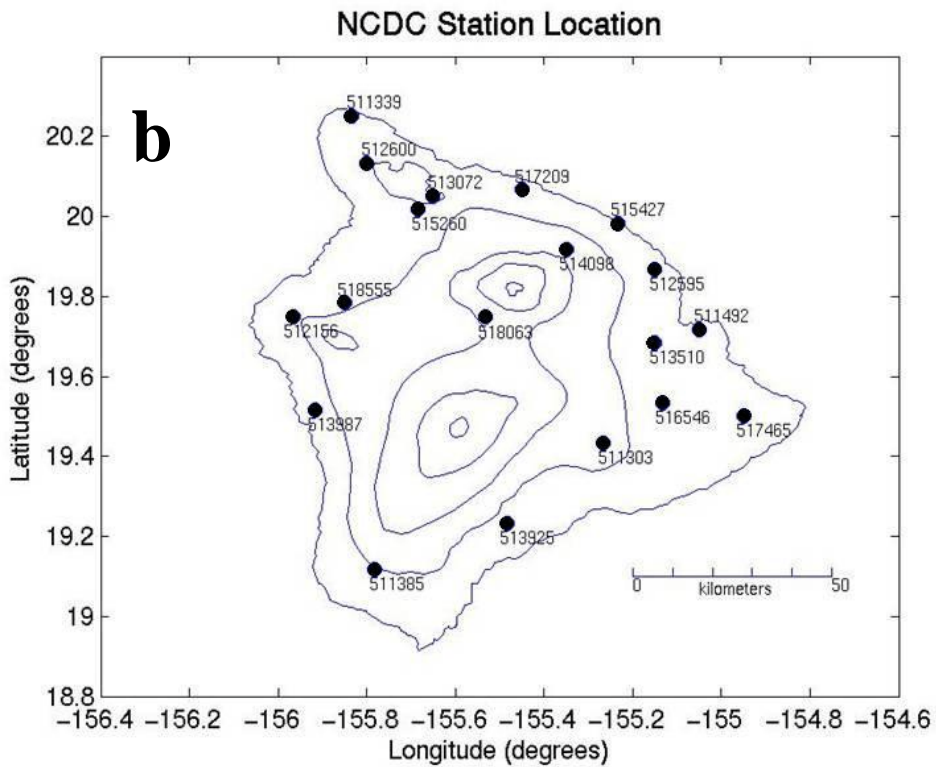


Figure 3b. Locations of National Climatic Data Center stations.

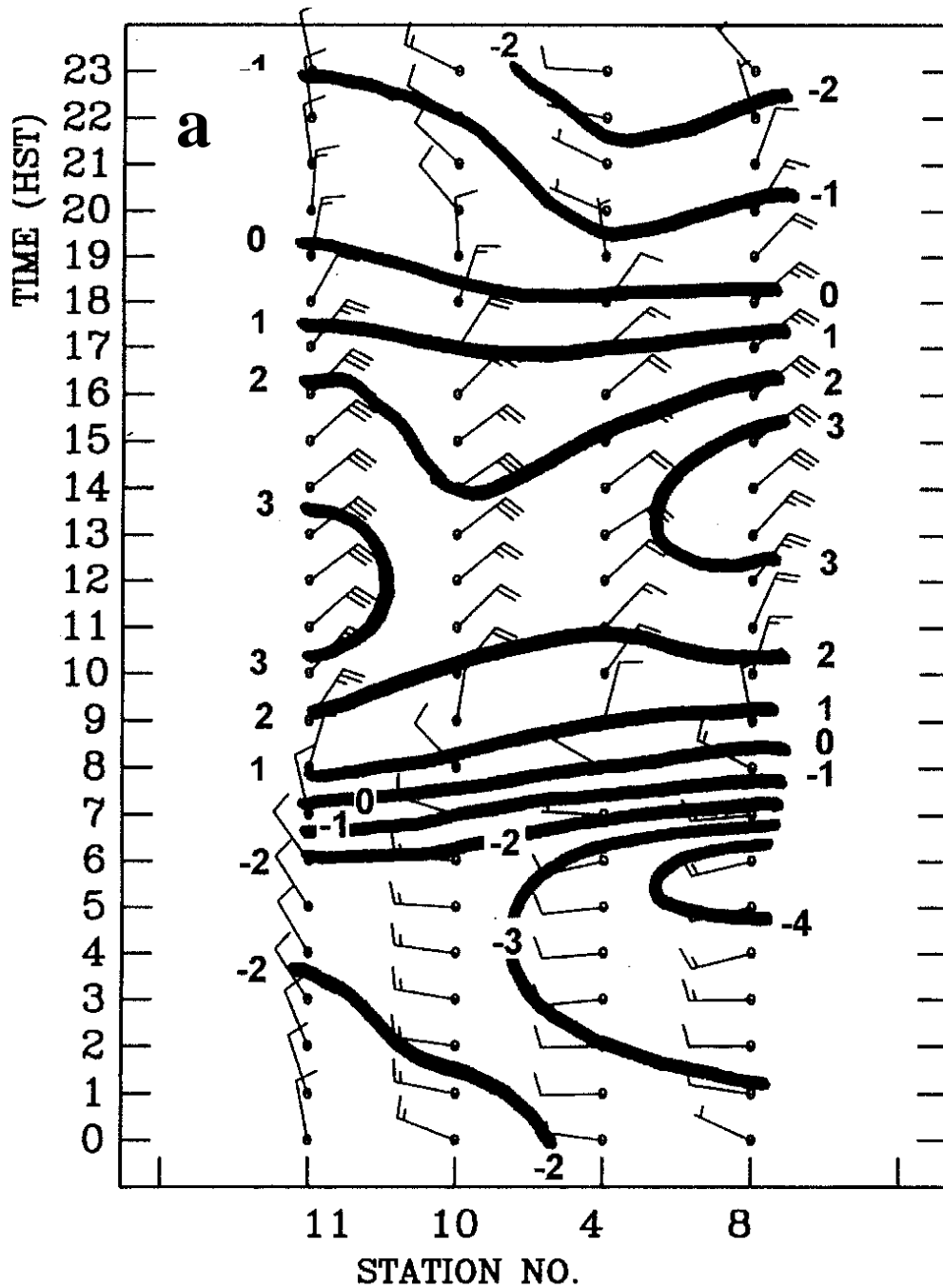


Figure 4a. Averaged winds and virtual temperature perturbation (ΔT_v) every 1 K between upstream and PAM data for transect from upper slopes to the coast of 45 HaRP days. Winds with one pennant, full barb, and half barb represent 5.0, 1.0, and 0.5 m s^{-1} respectively.

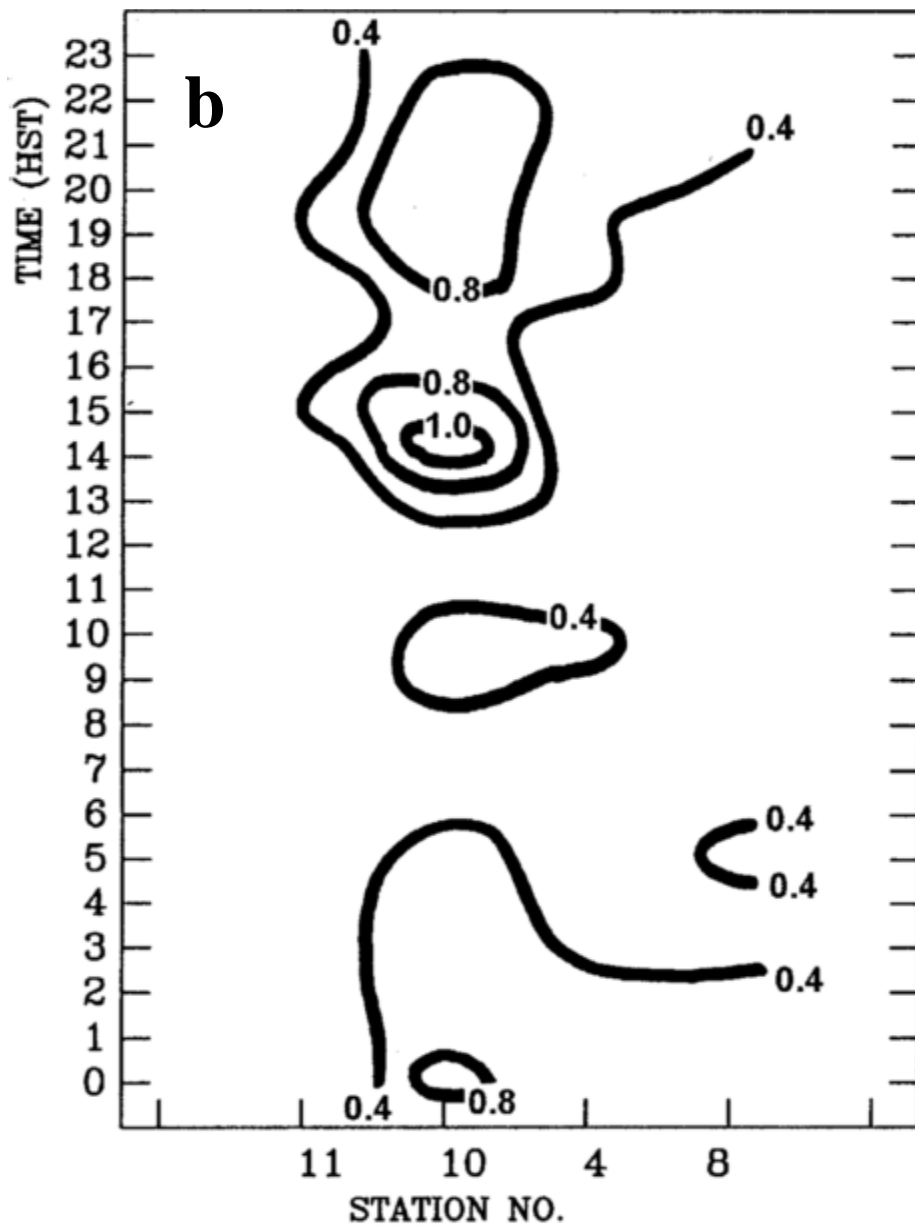


Figure 4b. Rainfall rate every 0.4 mm h⁻¹ for transect of windward coastal PAM stations of 45 HaRP days.

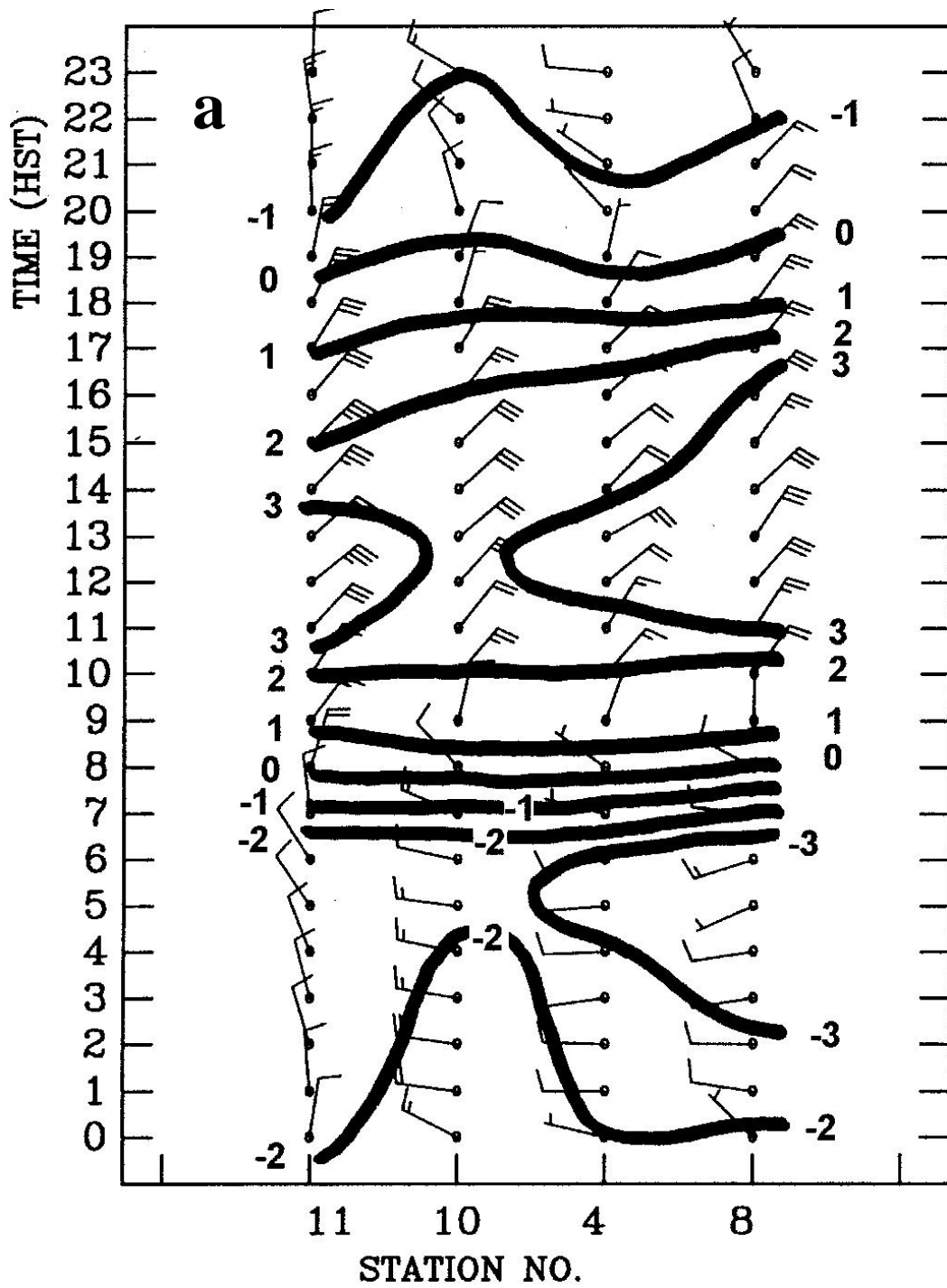


Figure 5a. Same as Figure 4a but for 12 strong trade-wind days.

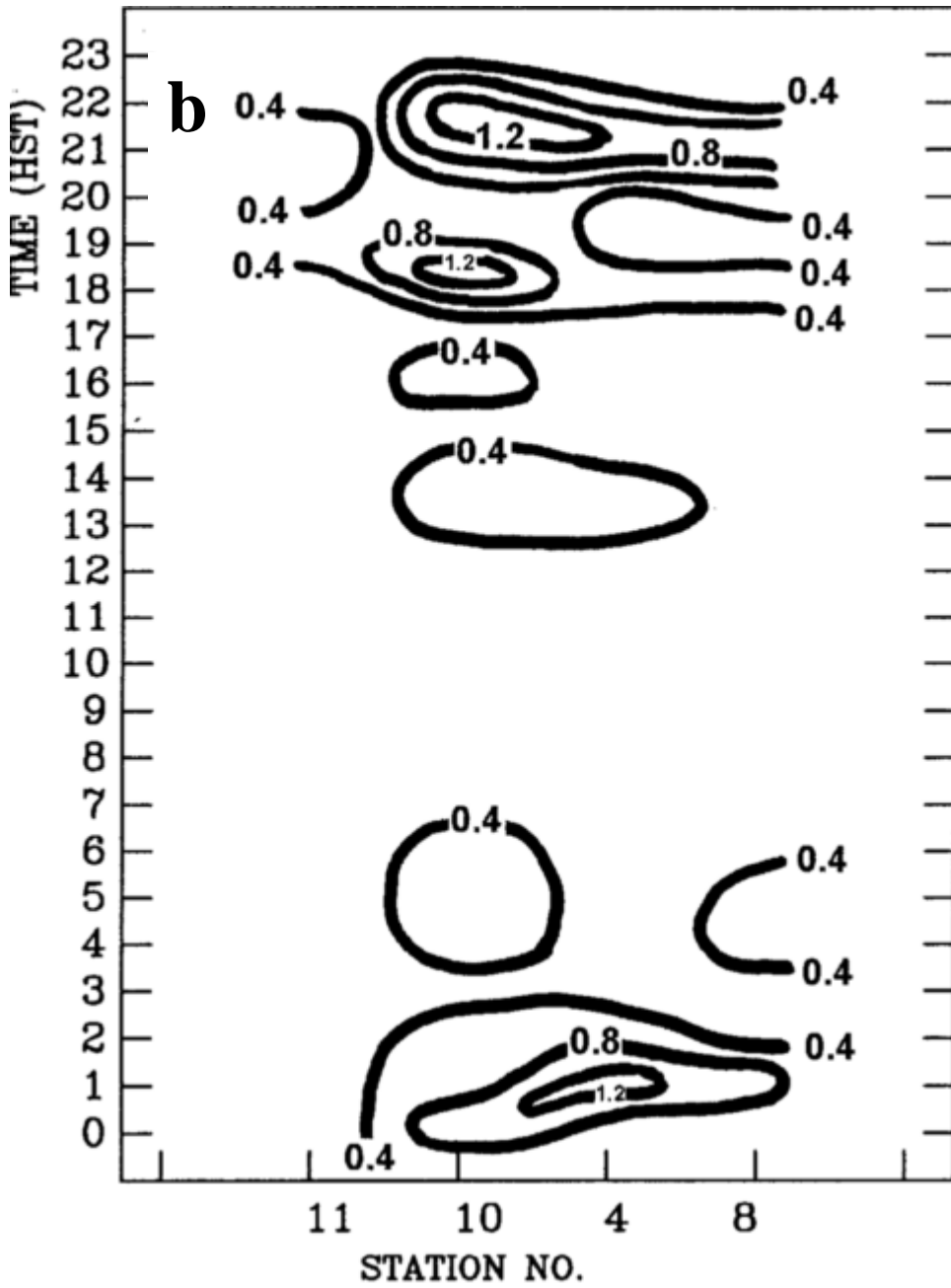


Figure 5b. Same as Figure 4b but for 12 strong trade-wind days.

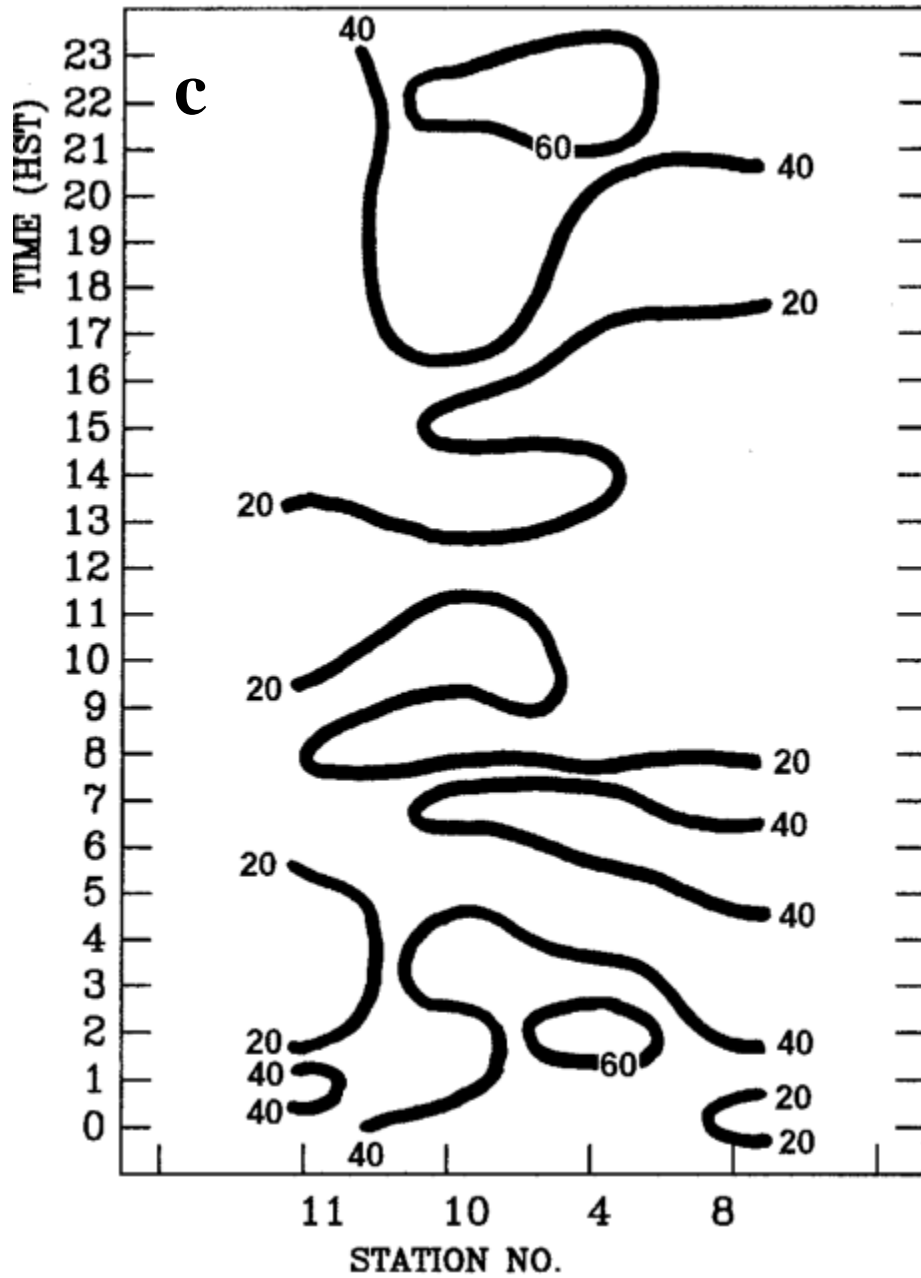


Figure 5c. Rainfall incidence (%) of strong trade-wind days. Contour intervals every 20%.

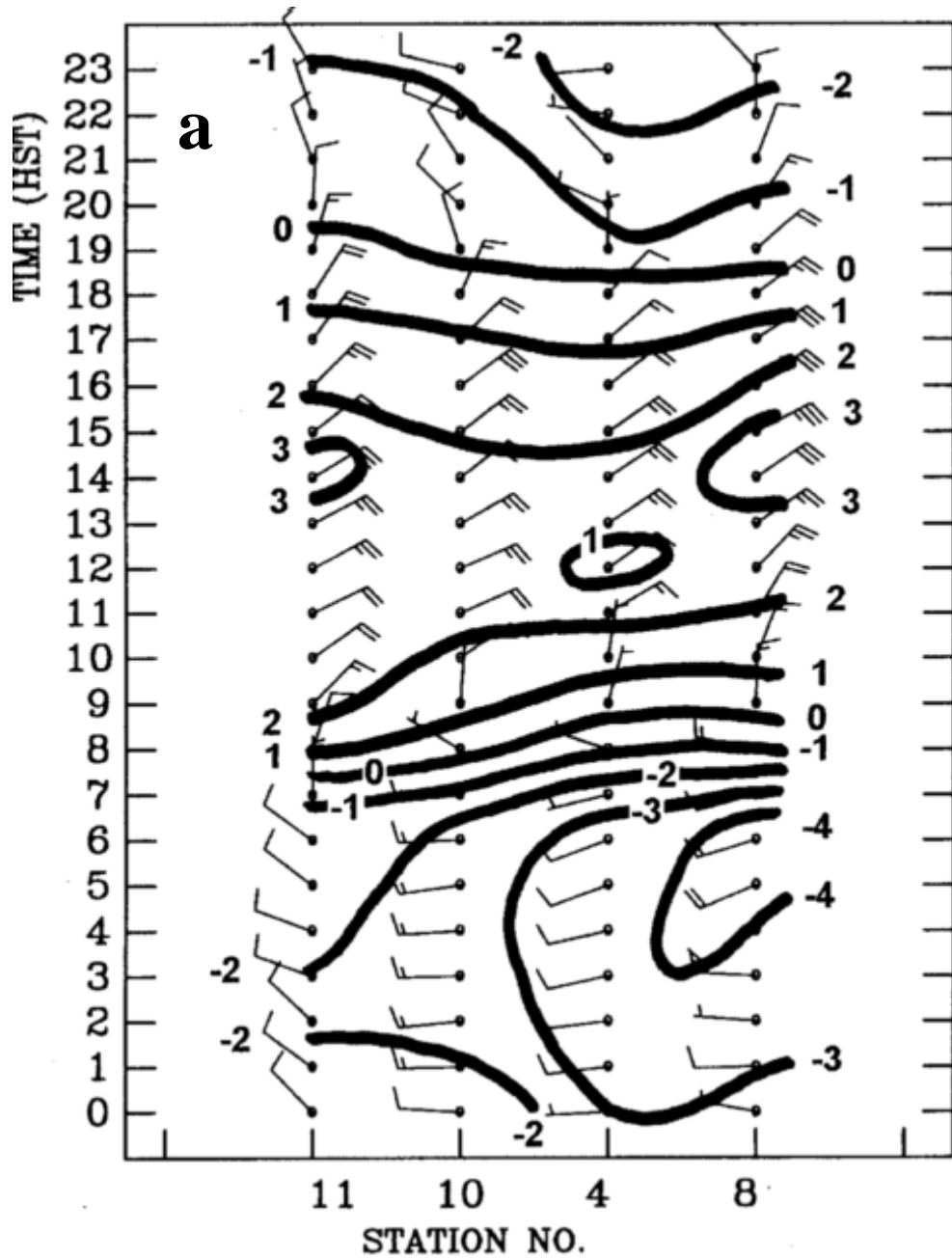


Figure 6a. Same as Figure 4a but for 12 weak trade-wind days.

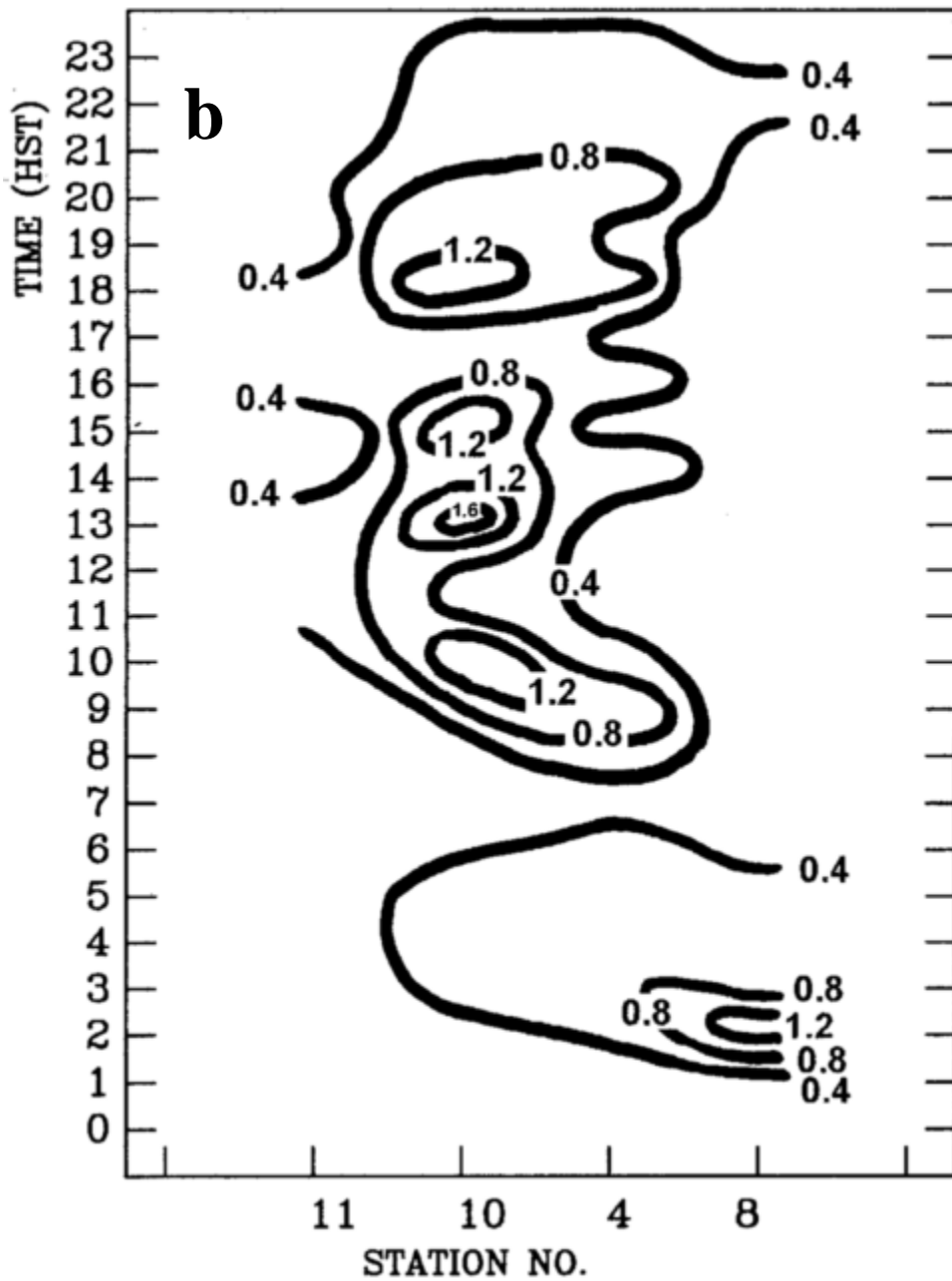


Figure 6b. Same as Figure 4b but for 12 weak trade-wind days.

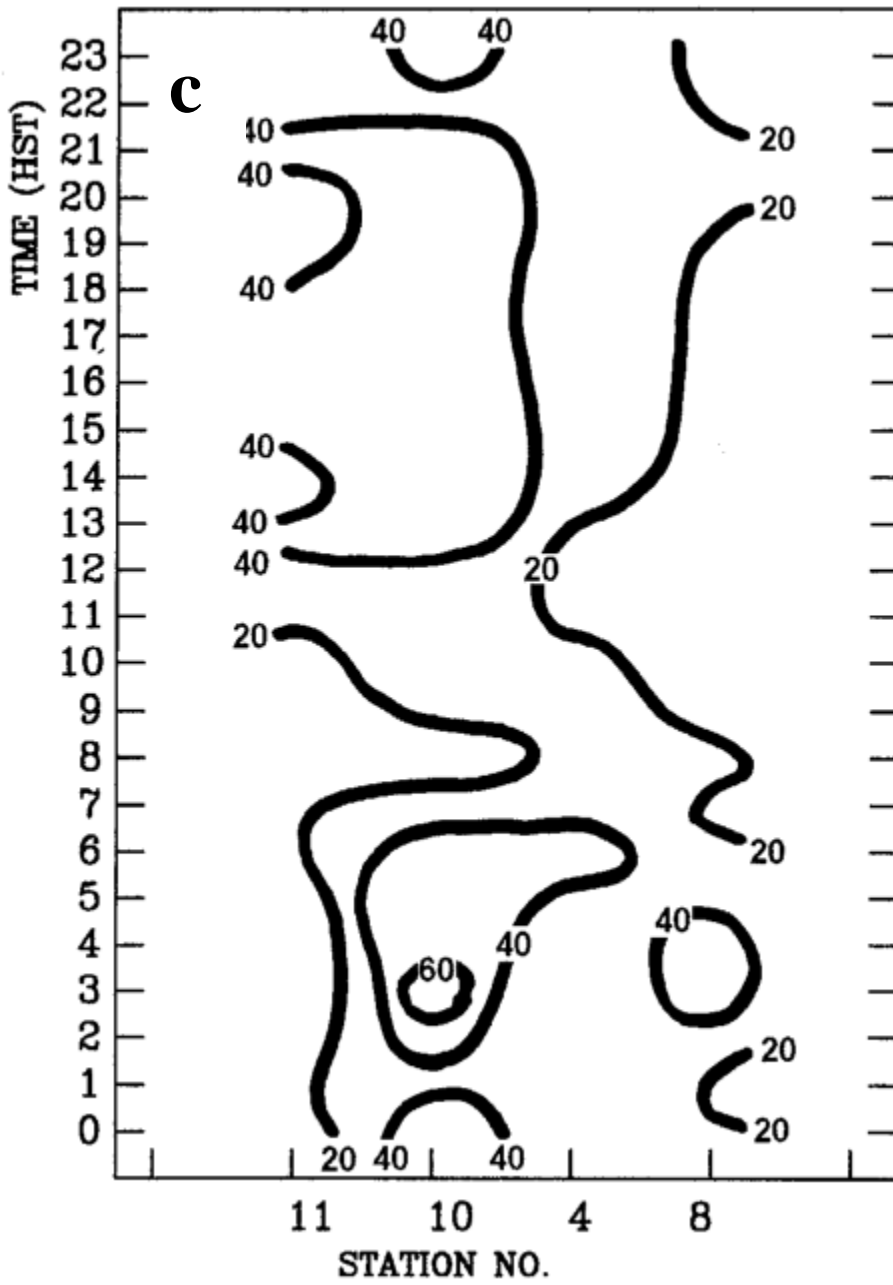


Figure 6c. Same as Figure 5c but for 12 weak trade-wind days.

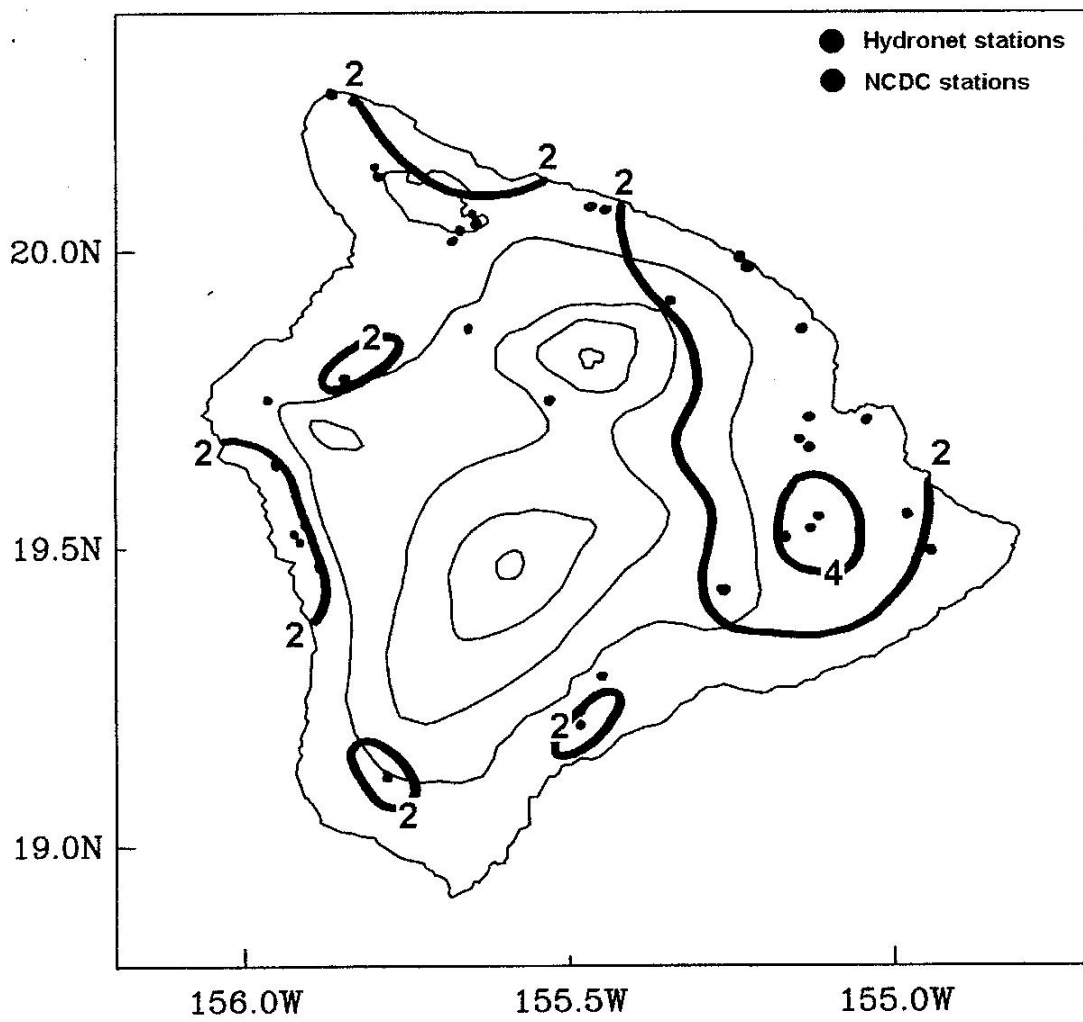


Figure 7a. Daily rainfall totals (mm day^{-1}) for weak trade-wind days. Terrain contours every 1 km.

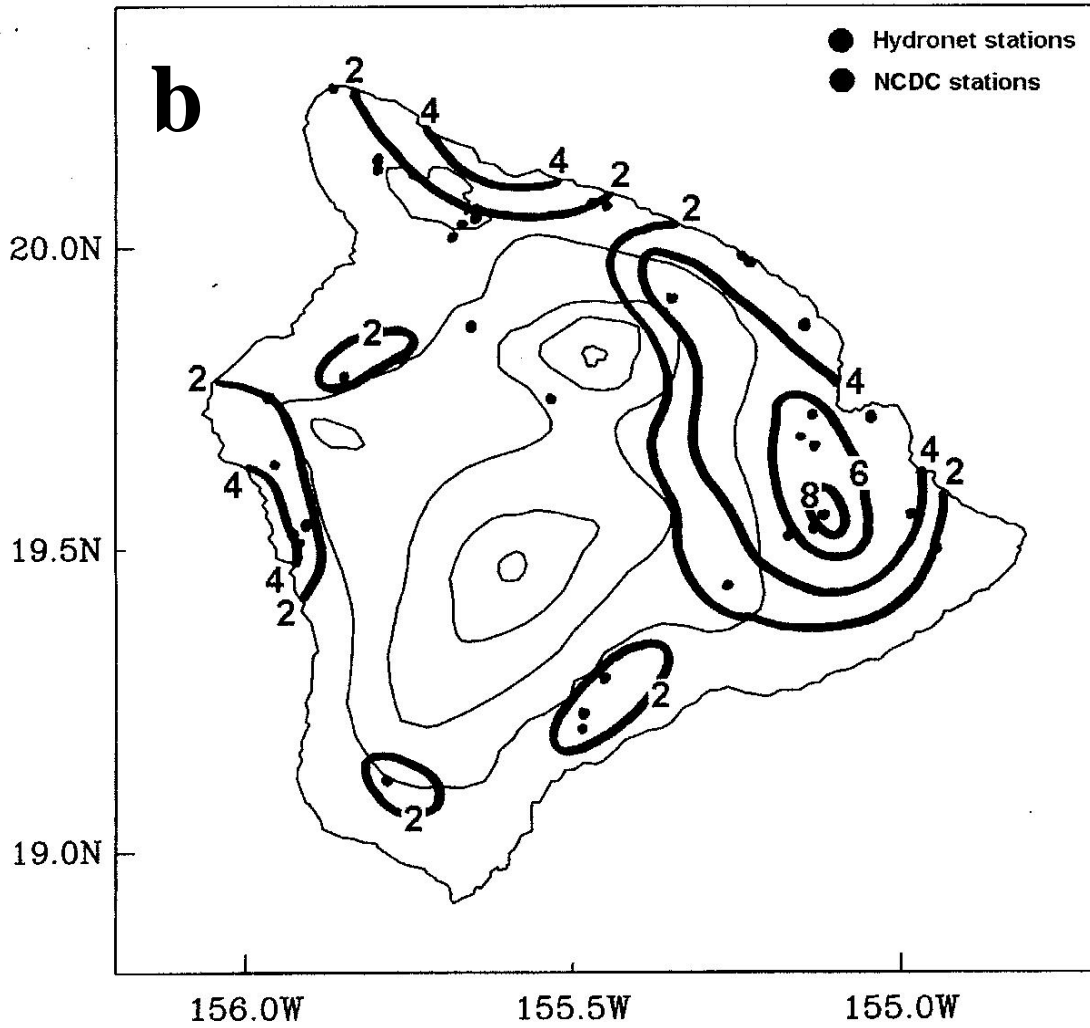


Figure 7b. Daily rainfall totals (mm day⁻¹) for moderate trade-wind days. Terrain contours every 1 km.

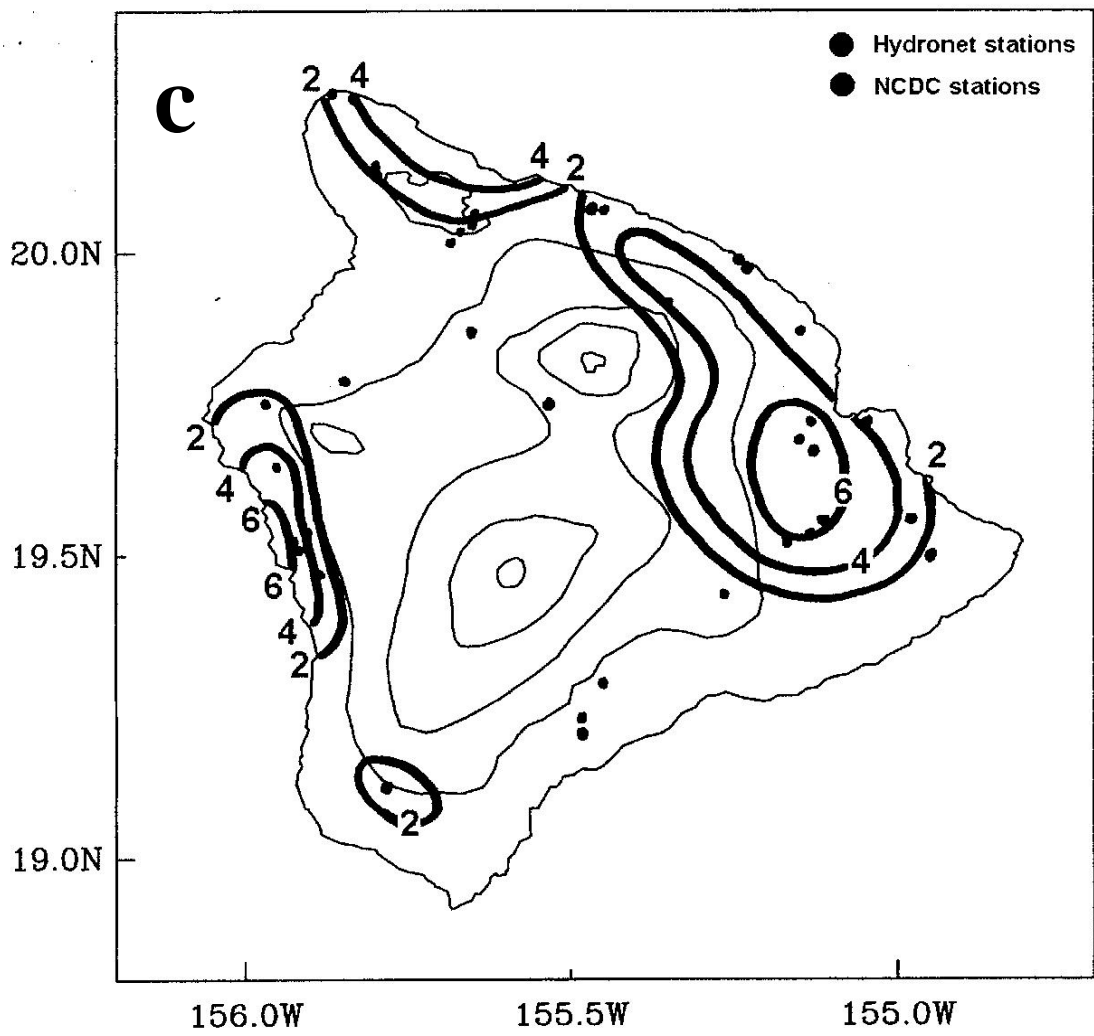


Figure 7c. Daily rainfall totals (mm day⁻¹) for strong trade-wind days.

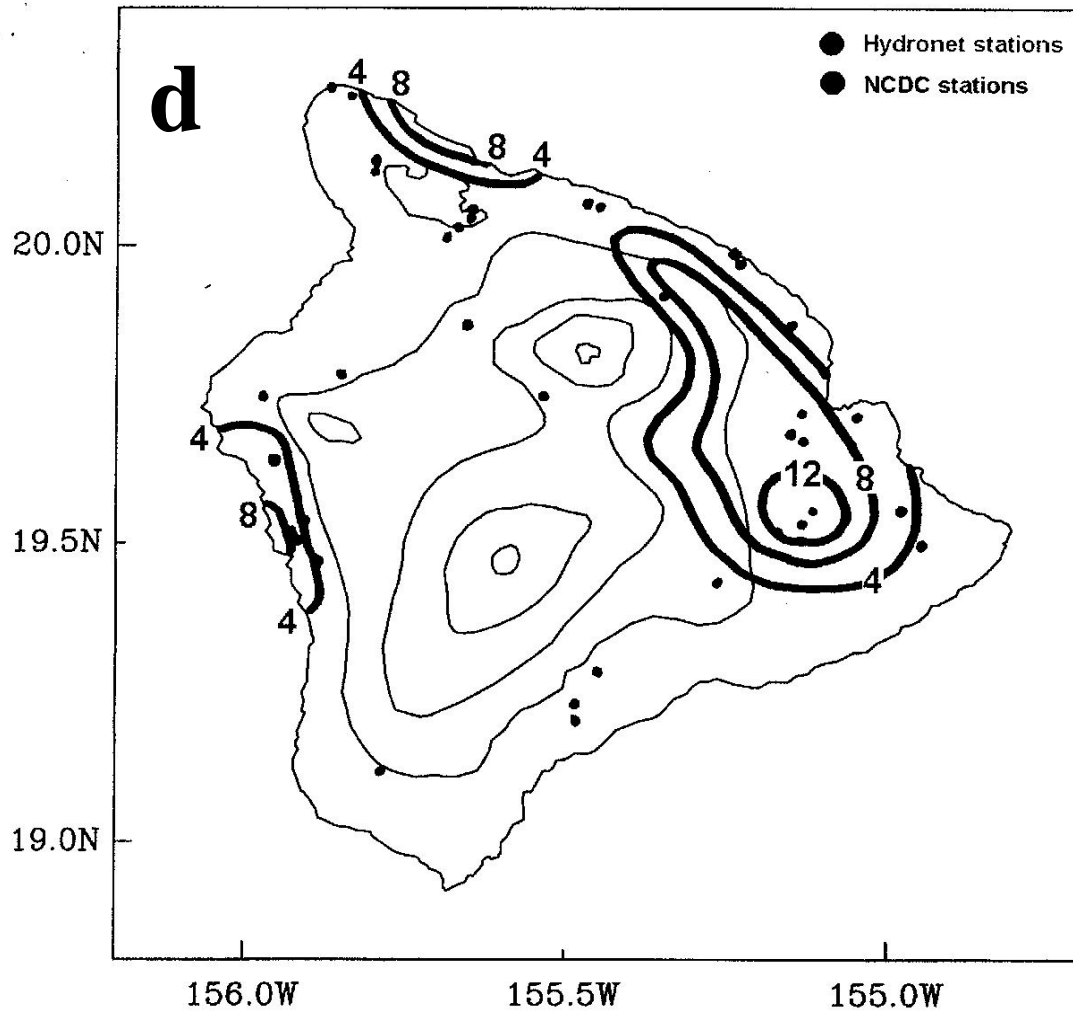


Figure 7d. Daily rainfall totals (mm day⁻¹) for moderately strong trade-wind days.

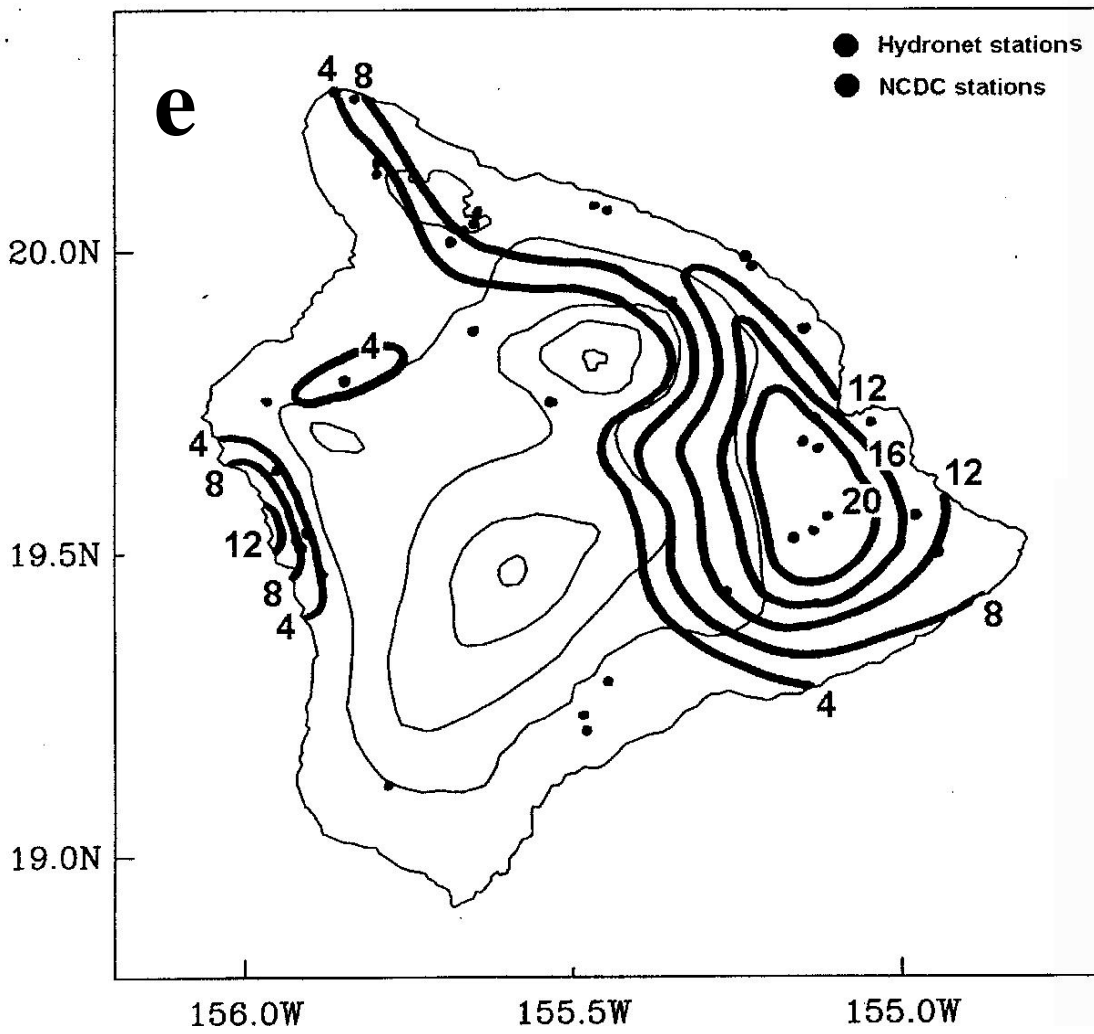


Figure 7e. Daily rainfall totals (mm day⁻¹) for very strong trade-wind days.

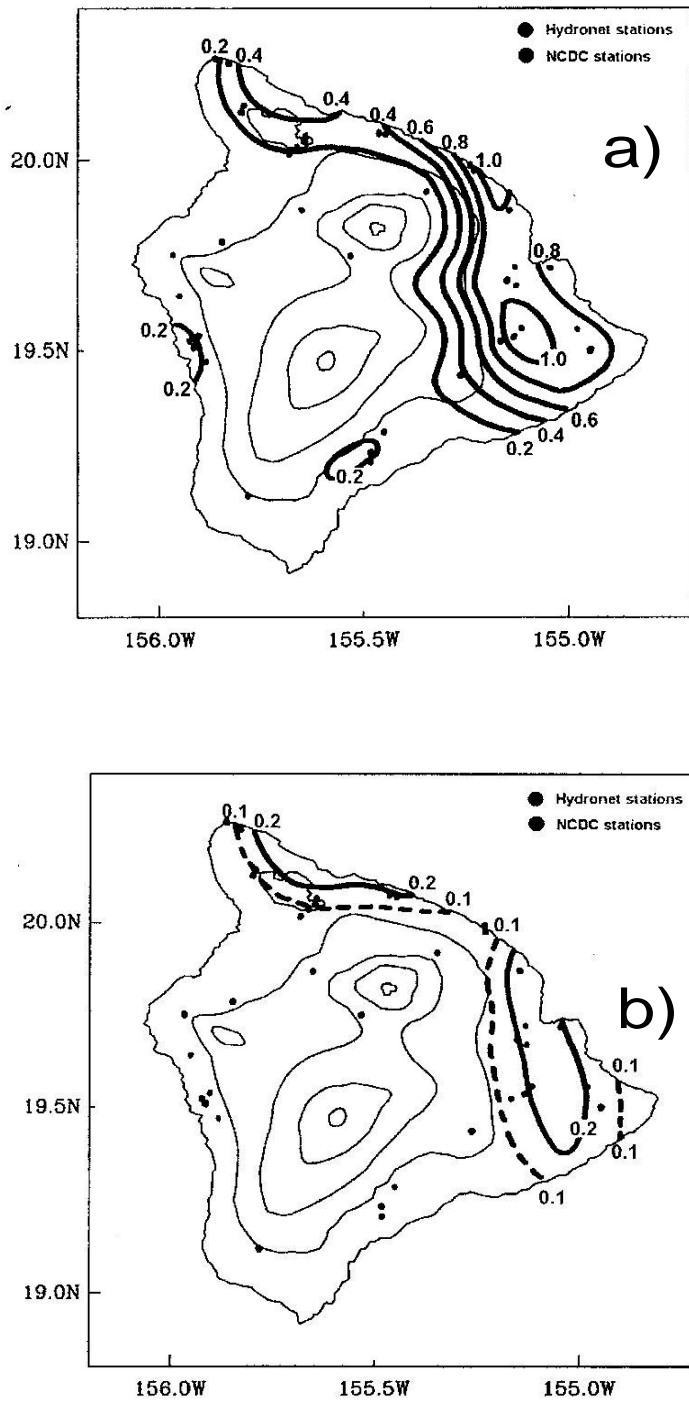


Figure 8. The rainfall rate (mm h⁻¹) for midnight (2300-0300 HST) for a) very strong and b) weak trade-wind regimes in 1997-2000.

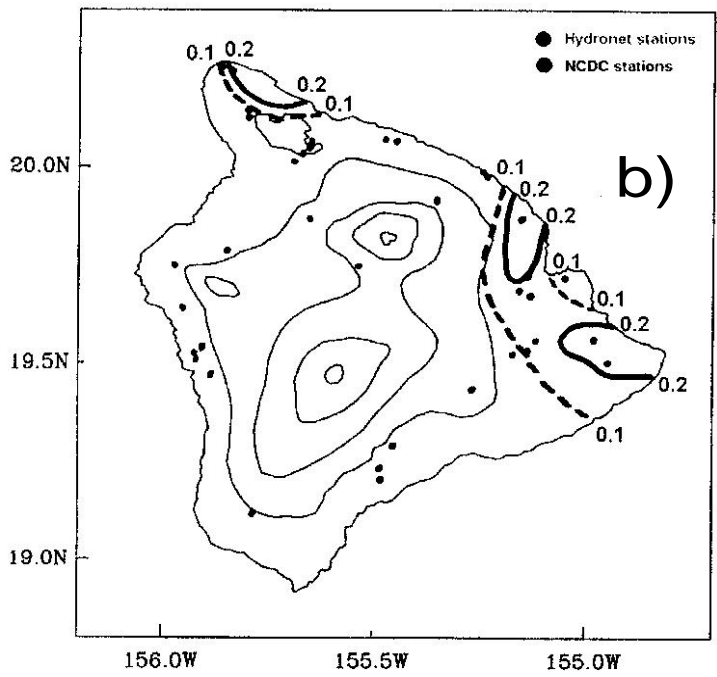
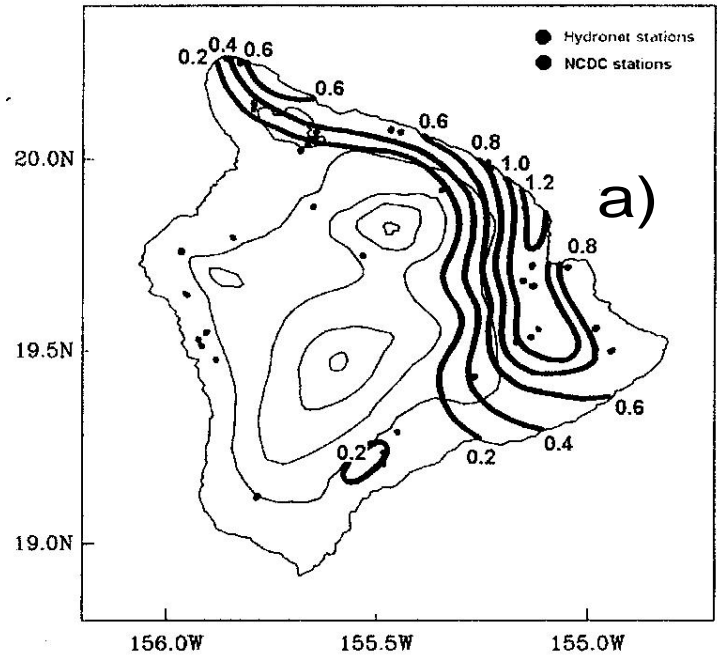


Figure 9. Same as Figure 8 but for 0300-0700 HST.

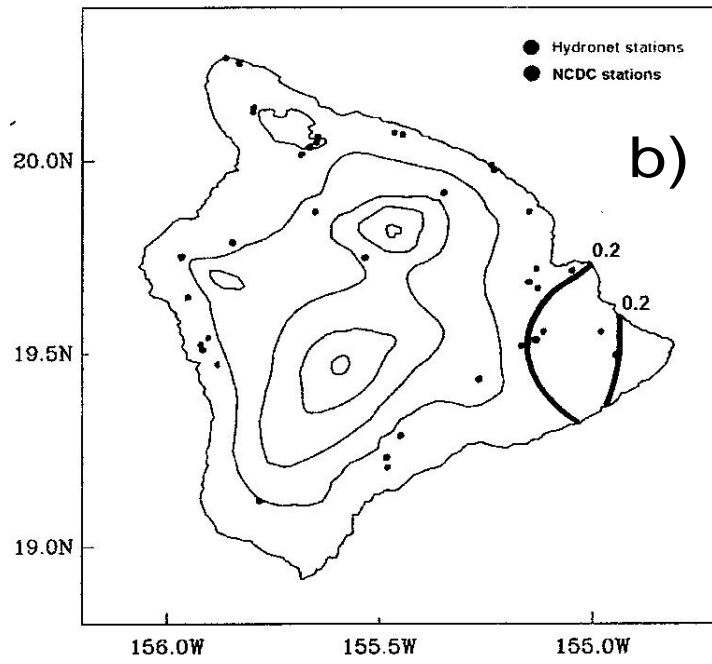
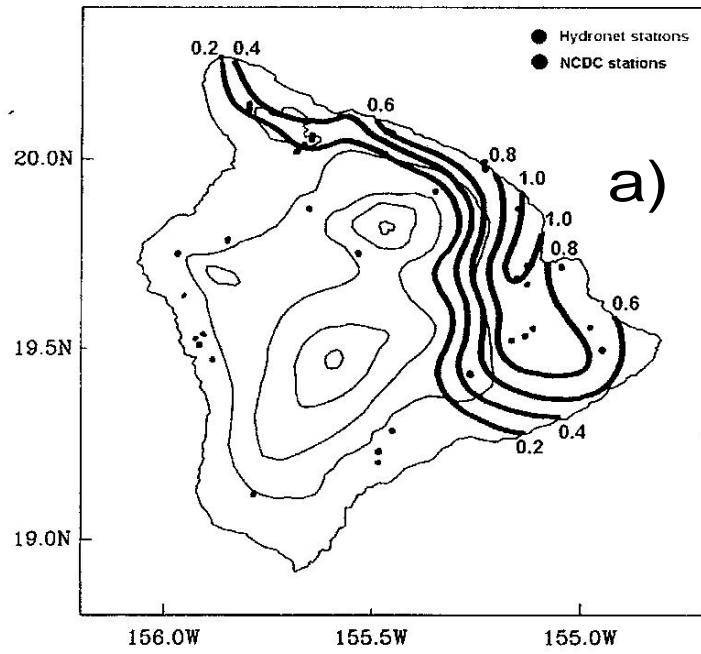


Figure 10. Same as Figure 8 but for 0700-1100 HST.

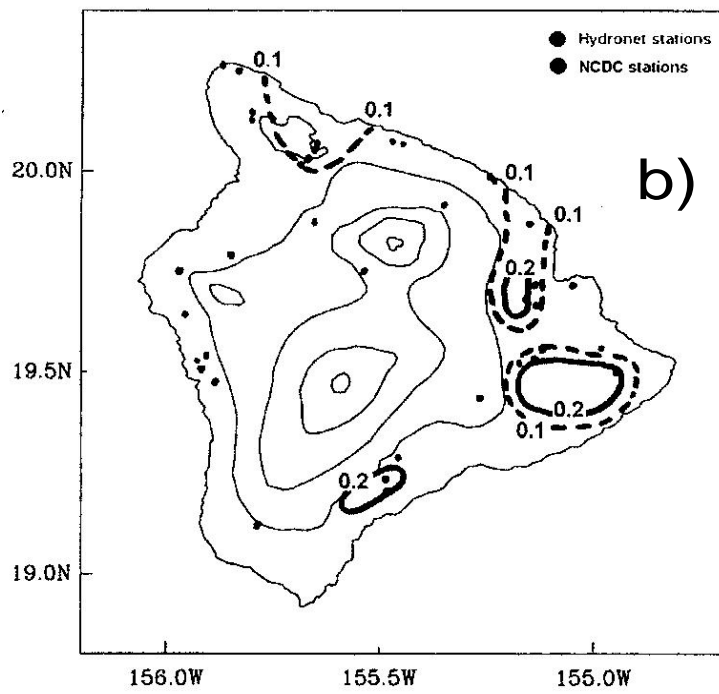
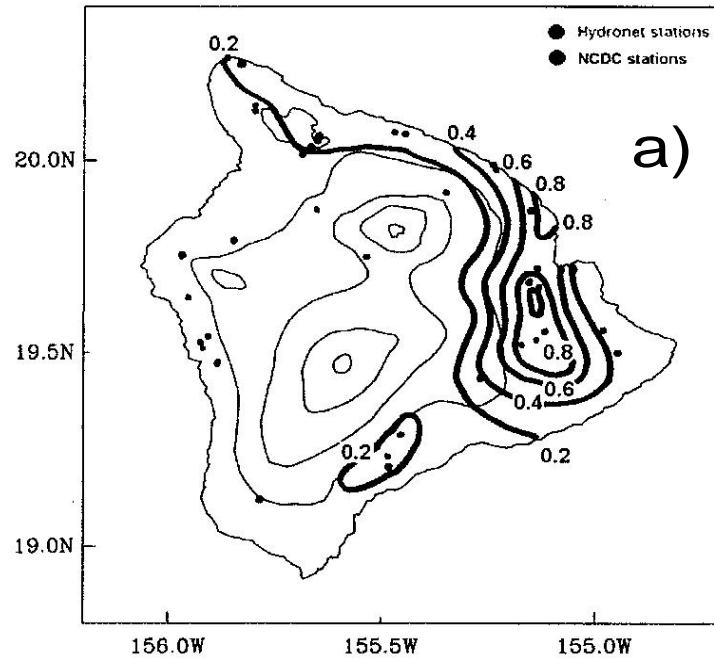


Figure 11. Same as Figure 8 but for 1100-1500 HST.

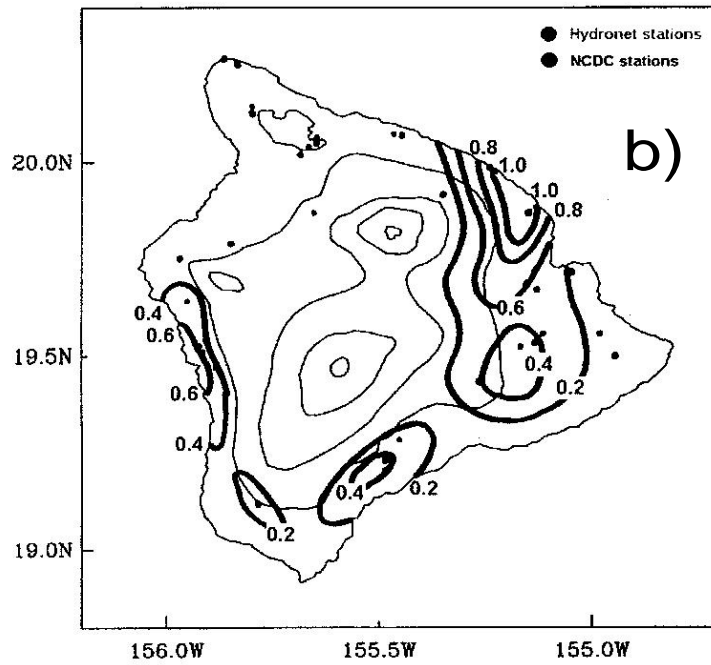
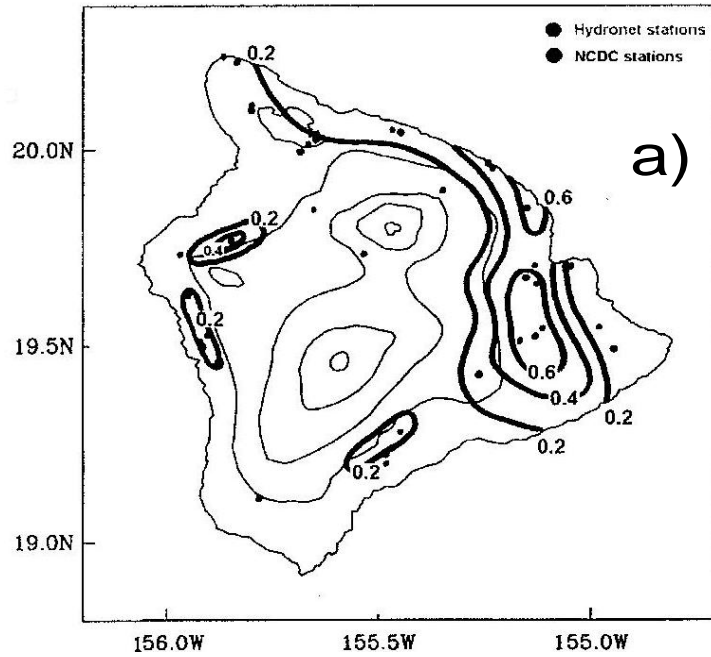


Figure 12. Same as Figure 8 but for 1500-1900 HST.

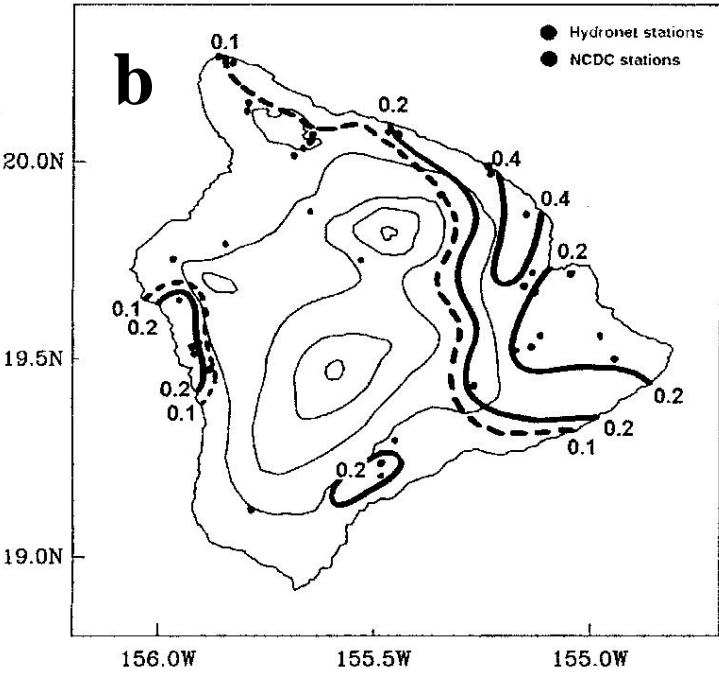
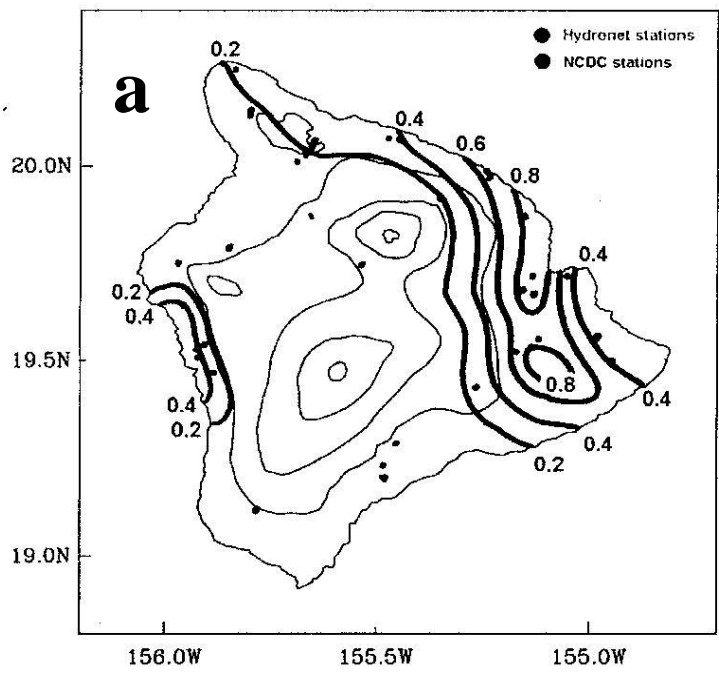


Figure 13. Same as Figure 8 but for 1900-2300 HST.